JM PAPERS

Bubble-induced transition to elasto-inertial turbulence

Hafiz Usman Naseer[1] , **Daulet Izbassarov**[2] , **Marco Edoardo Rosti**[3] and **Metin Muradoglu**[1]

[1]Department of Mechanical Engineering, Koç University, Istanbul 34450, Türkiye

[2]Finnish Meteorological Institute, Erik Palmenin aukio 1, Helsinki 00560, Finland

[3]Complex Fluids and Flows Unit, Okinawa Institute of Science and Technology Graduate University, 1919-1 Tancha, Onna-son, Okinawa 904-0495, Japan

Corresponding author: Metin Muradoglu, mmuradoglu@ku.edu.tr

Interface-resolved direct numerical simulations are performed to investigate bubble-induced transition from a laminar to elasto-inertial turbulent (EIT) state in a pressure-driven viscoelastic square channel flow. The Giesekus model is used to account for the viscoelasticity of the continuous phase, while the dispersed phase is Newtonian. Simulations are performed for both single- and two-phase flows for a wide range of Reynolds (Re) and Weissenberg (Wi) numbers. In the absence of any discrete external perturbations, single-phase viscoelastic flow is transitioned to an EIT regime at a critical Weissenberg number (Wi_{cr}) that decreases with increasing Re. It is demonstrated that injection of bubbles into a laminar viscoelastic flow introduces streamline curvature that is sufficient to trigger an elastic instability leading to a transition to an EIT regime. The temporal turbulent kinetic energy spectrum shows a scaling of -2 for this multiphase EIT regime, and this scaling is found to be independent of size and number of bubbles injected into the flow. It is also observed that bubbles move towards the channel centreline and form a string-shaped alignment pattern in the core region at the lower values of $Re = 10$ and $Wi = 1$. In this regime, there are disturbances in the core region in the vicinity of bubbles while flow remains essentially laminar. Unlike the solid particles, it is found that increasing shear-thinning effect breaks up the alignment of bubbles.

Key words: transition to turbulence, multiphase flow, viscoelasticity

H.U. Naseer, D. Izbassarov, M.E. Rosti and M. Muradoglu

1. Introduction

Adding a minute amount of long-chain flexible polymers can drastically change mechanical properties of an otherwise Newtonian fluid and makes it viscoelastic. Stretching of polymer molecules causes elastic stresses and gives a memory to the fluid flow, resulting in a range of exotic and often counter-intuitive behaviours such as rod climbing, elastic recoil and drag reduction in turbulent flows (Datta *et al.* 2022). The exact mechanism behind many of the exotic phenomena exhibited by the viscoelastic fluids are yet to be fully explored. A striking example of such phenomena is sustaining a chaotic, turbulent-like fluid motion observed at a low Reynolds number (Groisman & Steinberg 2000; Steinberg 2021; Datta *et al.* 2022; Singh *et al.* 2024). In the case of a classical Newtonian turbulent flow, the flow instabilities arise from the nonlinear convective terms of the Navier–Stokes equations and, therefore, a very high Reynolds number is always required to sustain a turbulent flow field. In the case of a viscoelastic fluid flow, however, the nonlinear coupling between viscous and viscoelastic stresses are capable of triggering and sustaining a chaotic motion even in the absence of inertia (Datta *et al.* 2022). This turbulent flow state at a Reynolds number below the threshold value of inertial turbulence (IT) is often referred to as the 'elasto-inertial turbulence' (EIT). When the Reynolds number is further reduced to a negligibly smaller value, it turns out that high enough viscoelastic stresses are still capable of sustaining a chaotic turbulent-like state, referred to as the elastic turbulence (ET), which is purely dominated by the elastic effects (Steinberg 2021). The present study mainly focuses on the elasto-inertial instability and transition to the elasto-inertial turbulence where, as the name implies, the chaotic flow state is caused and sustained by both elastic and inertial effects.

In the inertialess limit, only nonlinearity arises from the elastic stress that becomes anisotropic in a shear flow and results in the hoop stress acting on the fluid in the direction of the streamline curvature. This hoop stress provides the driving force for the elastic instability and triggers a transition to the elastic turbulent state even in the absence of inertia (Steinberg 2021). Since the discovery of ET in inertialess flows with curved streamlines by Groisman & Steinberg (2000), a nonlinear instability leading to a similar kind of chaotic state in planar shear flows was suspected and investigated by Morozov & van Saarloos (2005, 2019). These studies suggested that a nonlinear instability can also be triggered in a planar shear flow when a sufficient flow curvature is induced via external perturbations. To realise this, the initial perturbations have been usually induced in the form of blowing/suction at the wall or by placing an obstacle in the channel to trigger the instability and attain an EIT state (Dubief, Terrapon & Hof 2023).

There are different pathways which can be followed to achieve the EIT state in a wall-bounded flow. Samanta *et al.* (2013) have demonstrated that the transition threshold to inertial turbulence can be controlled by varying the polymer concentration. They computed the puff lifetimes to examine the effects of viscoelasticity on transition and differentiate the EIT states from the Newtonian turbulence in a pipe flow. They found that polymer additives delay the subcritical transition to IT conforming to their drag-reducing effects in turbulent channel flows. They also demonstrated that, as the shear rate is increased, a separate instability occurs at a much lower Reynolds number than the inertial turbulence and triggers a very different type of disordered motion of elasto-inertial turbulence. Foggi Rota *et al.* (2024) showed that a reverse pathway can also be followed to achieve the EIT state. That is, viscoelasticity is introduced into an already turbulent Newtonian flow and then the Reynolds number is reduced gradually. Unlike the Newtonian flow, which would immediately re-laminarise below a certain threshold value of *Re*, the viscoelastic flow is capable of maintaining its turbulent state even at a Reynolds number as low as $Re = 0.5$ in a rectilinear channel. Moreover, at a low Reynolds

number, if some external perturbations are superimposed on a laminar viscoelastic flow field, these instabilities can grow and achieve the EIT state under a certain parametric setting (Garg *et al.* 2018; Beneitez *et al.* 2023, 2024).

The dynamic features of EIT differ greatly from the inertial turbulence, which is the focus of many contemporary investigations. Sid, Terrapon & Dubief (2018) have demonstrated that the essential dynamic structures of EIT exist even in a two-dimensional (2-D) flow. More recently, Dubief *et al.* (2022) have identified four distinct regimes of the stress field in a 2-D channel flow by using the FENE-P viscoelastic model. These regimes were named as chaotic, chaotic arrowhead, intermittent arrowhead and stable arrowhead regimes based on constant contours of first normal stress difference (N_1) and pressure field. A sharp pressure gradient was observed within the flow field, similar to that across a shock wave, promoting the shape of an arrowhead. In this 2-D flow field, it was reported that an increase in the polymer concentration promoted stability while an increase in the domain length promoted chaos, indicating the role of large scales in the dynamics of EIT. The drag was found to be increasing in all these EIT regimes when compared with the corresponding laminar states. In a three-dimensional (3-D) periodic channel flow, Dubief *et al.* (2010) observed an alternating train of positive and negative Q-iso-surfaces (second invariant of velocity gradient tensor) near the channel wall during transition to the EIT state. Interestingly, these patterns were sustained on a smaller scale unlike the inertial turbulence even when the viscoelastic flow was fully developed. These patterns were interpreted as the regions of local rotation ($Q > 0$) and dissipation of turbulent kinetic energy ($Q < 0$), and were found to change their alignment from streamwise to spanwise direction during low-drag events. Another striking difference between IT and EIT is the reversed energy cascade. Unlike the inertial turbulence where the energy transfer occurs from large to small scales, energy transfer of turbulent elastic energy to turbulent kinetic energy is observed to be from smaller to larger scales in EIT (Dubief, Terrapon & Soria 2013).

Despite an ever increasing interest in this area in recent years, many fundamental aspects related to EIT are still elusive. In the present study, we focus on two such aspects. First, instead of providing any external perturbations to the flow, direct numerical simulations of concentrated viscoleastic flows are performed in a square-shaped channel by gradually increasing the fluid elasticity while keeping the Reynolds number fixed at a low value for which the corresponding Newtonian flow is fully laminar to examine the conditions for attaining an EIT state. Second, a novel mechanism of injecting bubbles into a laminar viscoelastic flow is investigated to ascertain whether the presence of bubbles can trigger a transition to an EIT state in this straight channel. For this purpose, extensive interface-resolved direct numerical simulations are performed using a finite-difference/front-tracking method (Unverdi & Tryggvason 1992). The log-conformation method (Fattal & Kupferman 2005) is employed to handle the stiff constitutive equations of the viscoelastic model (Giesekus) at high Weissenberg numbers.

The numerical method and the computational set-up are described in §§ 2 and 3, respectively. The results are presented and discussed for a single-phase and then for the multiphase flows in § 4, followed by the conclusions in § 5.

2. Governing equations and numerical method

The flow equations and the Giesekus model are presented within the framework of the finite-difference/front-tracking (FT) method. The front-tracking method used in the present study was originally developed by Unverdi & Tryggvason (1992). Izbassarov & Muradoglu (2015) added a capability to this FT method to simulate viscoelastic two-phase systems in which one or both phases could be viscoelastic. This robust and high fidelity

method has been extensively used in our several previous works involving laminar (e.g. Izbassarov & Muradoglu 2016*a*, *b*; Naseer *et al.* 2023; Naseer *et al.* 2024) as well as turbulent multiphase flows (e.g. Ahmed *et al.* 2020; Izbassarov *et al.* 2021*a*). Referring to the coordinate system shown in figure 1 and employing the one-field formulation, the Navier–Stokes equations can be written as

$$\rho \frac{\partial \boldsymbol{u}}{\partial t} + \rho \nabla \cdot (\boldsymbol{uu}) = -\nabla p - \frac{\mathrm{d}p_o}{\mathrm{d}y} \boldsymbol{j} + \nabla \cdot \boldsymbol{\tau} + \nabla \cdot \mu_s (\nabla \boldsymbol{u} + \nabla \boldsymbol{u}^T)$$
$$+ \int_A \sigma \kappa \boldsymbol{n} \delta(\boldsymbol{x} - \boldsymbol{x}_f) \, \mathrm{d}A, \tag{2.1}$$

where $\boldsymbol{u}$, $\boldsymbol{\tau}$, p, ρ and μ_s are the velocity vector, the polymer stress tensor, the pressure, and the discontinuous density and solvent viscosity fields, respectively. A pressure gradient $-(\mathrm{d}p_o/\mathrm{d}y)\boldsymbol{j}$ is applied to drive the flow and it is adjusted dynamically to keep the flow rate constant, where $\boldsymbol{j}$ is the unit vector in the y-direction. The effect of surface tension is added as a body force term on the right-hand side of the momentum equation, where σ is the surface tension coefficient, κ is twice the mean curvature and $\boldsymbol{n}$ is a unit vector normal to the interface. As the surface tension acts only on the interface, δ represents a three-dimensional Dirac delta function with the arguments $\boldsymbol{x}$ and $\boldsymbol{x}_f$ being a point at which the equation is evaluated and a point at the interface, respectively. The momentum equation is supplemented by the incompressibility condition

$$\nabla \cdot \boldsymbol{u} = 0. \tag{2.2}$$

Viscoelasticity of bulk liquid is modelled using the Giesekus model (Giesekus 1982). Since this model accounts for the polymer–polymer interactions, it is a suitable choice to simulate concentrated polymer solutions (Varchanis *et al.* 2022). In the Giesekus model, the polymer stress tensor $\boldsymbol{\tau}$ evolves by

$$\boldsymbol{\tau} = \frac{\mu_p}{\lambda} (\boldsymbol{B} - \boldsymbol{I}), \tag{2.3}$$

where μ_p is the polymer viscosity, λ is the polymer relaxation time, $\boldsymbol{B}$ is the conformation tensor and $\boldsymbol{I}$ is the identity tensor. The conformation tensor evolves by

$$\frac{\partial \boldsymbol{B}}{\partial t} + \boldsymbol{u} \cdot \nabla \boldsymbol{B} - \nabla \boldsymbol{u}^T \cdot \boldsymbol{B} - \boldsymbol{B} \cdot \nabla \boldsymbol{u} = \frac{1}{\lambda} \left[(1-\alpha)\boldsymbol{I} + (2\alpha-1)\boldsymbol{B} - \alpha \boldsymbol{B}^2 \right], \tag{2.4}$$

where α is the mobility factor representing the anisotropy of the hydrodynamic drag exerted on the polymer molecules. Due to the thermodynamic considerations, α is restricted to $0 \leqslant \alpha \leqslant 0.5$ (Schleiniger & Weinacht 1991). When $\alpha = 0$, the Giesekus model reduces to the Oldroyd-B model.

At high Weissenberg numbers, these highly nonlinear viscoelastic constitutive equations become extremely stiff, which makes their numerical solution a challenging task. Artificial diffusion terms may be added to the discretised viscoelastic model equations to alleviate this problem. However, it has been found that when the model equations are discretised using the conventional numerical schemes, this artificial diffusion method may alter the mathematical nature of the constitutive equations from hyperbolic to parabolic, affecting the integrity of the simulated EIT physics, especially at high Weissenberg numbers (Dubief *et al.* 2023). The log-conformation method offers an alternative solution to this problem and it is used in the present study. In this approach, an eigen decomposition is employed to re-write the constitutive equation of the conformation tensor (Fattal & Kupferman 2005; Izbassarov *et al.* 2018). It is found that, although it is computationally more expensive than the artificial diffusion method, the log-conformation retains the hyperbolic nature
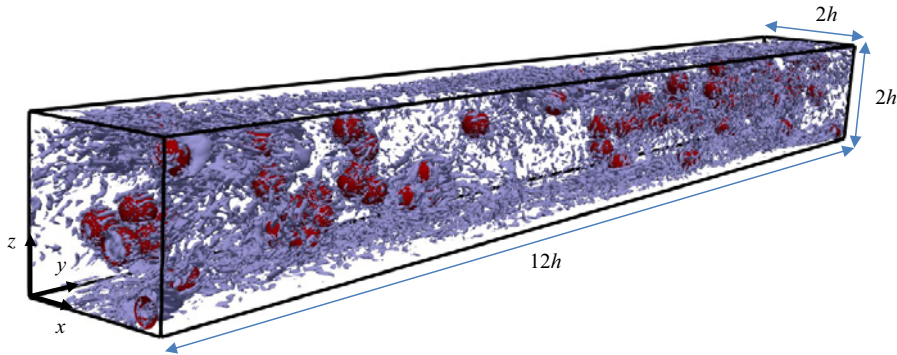
Figure 1. Computational domain and coordinate system considered in the present study. The constant contours of Q-criterion are shown around the bubbles (red colour) at a value of $Q = 25$ ($Re = 1000$, $Wi = 10$, $Ca = 0.01$, $\beta = 0.1$).

and thus removes the stiffness of the viscoelastic model equations, allowing robust and accurate numerical solutions by preserving large-scale features in the simulations of elastic turbulence, as shown recently by Yerasi *et al.* (2024). The interested readers are referred to Fattal & Kupferman (2005) for the details of the procedure.

The flow equations (2.1) and (2.2) are solved fully coupled with the Giesekus model equation (2.3). A QUICK scheme is used to discretise the convective terms in the momentum equations, while second-order central differences are used for the diffusive terms. For the convective terms in the viscoelastic equations, a fifth-order WENO-Z (Borges *et al.* 2008) scheme is used. An FFT-based solver is employed to solve the pressure Poisson equation. Since the pressure equation is not separable due to variable density in the present multiphase flow, the FFT-based solvers cannot be used directly. To overcome this challenge, a pressure-splitting technique presented by Dong & Shen (2012) and Dodd & Ferrante (2014) is employed. A predictor-corrector scheme is used to achieve second-order time accuracy as described by Tryggvason *et al.* (2001). The details of the front-tracking method can be found in the book by Tryggvason, Scardovelli & Zaleski (2011) and in the review paper by Tryggvason *et al.* (2001), and the treatment of the viscoelastic model equations in Izbassarov & Muradoglu (2015) and Izbassarov *et al.* (2018). The present numerical scheme is second-order accurate both in space and time.

3. Computational set-up

Figure 1 shows the computational domain which is a square channel with the dimensions of $2h \times 12h \times 2h$ in the x, y and z directions, respectively, where h is half of the channel width. Periodic boundary conditions are applied in the streamwise (y) direction, whereas the other two directions (x and z) have no-slip/no-penetration boundary conditions. The length of the channel is set to $12h$ so that a sufficient length is available for the bubbles to exhibit their effects in the viscoelastic flow field.

The flow conditions are characterised by the following non-dimensional numbers defined as

$$Re = \frac{\rho_o u_o h}{\mu_o}, \quad Wi = \frac{\lambda u_o}{h}, \quad Ca = \frac{\mu_o u_o}{\sigma}, \quad \beta = \frac{\mu_s}{\mu_o}, \tag{3.1}$$

where Re, Wi and Ca are the Reynolds, Weissenberg and capillary numbers, respectively. Further, β is the ratio of the solvent viscosity (μ_s) to the zero shear viscosity (μ_o) of the viscoelastic fluid. In (3.1), ρ_o is the density of the bulk fluid and u_o is the average velocity

in the channel. The viscosity ratio is fixed at $\beta = 0.1$, representing a highly concentrated polymer solution, for all the results presented in this paper.

The present study covers the Reynolds and the Weissenberg numbers spanning in the ranges of $10 \leqslant Re \leqslant 1000$ and $1 \leqslant Wi \leqslant 1000$. Note that the highest value of $Re = 1000$ is still less than the minimum value required to sustain inertial turbulence in a channel flow (Owolabi, Poole & Dennis 2016). For these low values of Re, the grid resolution near the wall cannot be determined by the classical wall criterion of $x^+ < 1$ and $z^+ < 1$. As the bubbles are also injected into the flow, despite a low Re, a sufficiently fine grid is required to resolve the bubble interfaces and to capture the essential flow features of this chaotic viscoelastic flow regime. Therefore, a grid size of $320 \times 960 \times 320$ is used in the x, y and z directions even for the $Re = 10$ case. For a reference, this grid resolution is sufficient to achieve $x^+ < 0.8$ and $z^+ < 0.8$ in an inertial turbulent channel flow at $Re = 5600$ ($Re_\tau = 180$). For the multiphase cases, there are 64 grid cells per equivalent bubble diameter with this selected grid size.

The flow is driven by applying $\mathrm{d}p_o/\mathrm{d}y$ in the negative y-direction. This external pressure gradient is adjusted dynamically at each time step to keep the flow rate (and thus the bulk Reynolds number) constant in the channel. To normalise various quantities reported in this study, h is used as the length scale, u_o as the velocity scale and h/u_o as the time scale. The normalised quantities are denoted by the superscript *. The stresses are normalised by $\rho_o v_\tau^2$, where $v_\tau = \sqrt{\bar{\tau}_w/\rho_o}$ with $\bar{\tau}_w$ being the average total wall shear stress. Once the flow reaches a statistically steady state, the combined force due to the shear stresses at the four walls of the channel is balanced by the force due to the applied pressure gradient $\mathrm{d}p_o/\mathrm{d}y$. In this multiphase flow, the density and viscosity of the bubble are denoted by ρ_i and μ_i, respectively. The density and the viscosity ratios are set to $\rho_o/\rho_i = 10$ and $\mu_o/\mu_i = 80$, respectively. These comparatively small ratios are used to enhance numerical stability and thus relax the time step restrictions. Apparently, this low density ratio may seem unrealistic when compared with a liquid–air system. However, a higher density ratio does not affect the bubble dynamics significantly as has been reported by Bunner & Tryggvason (2002) for a Newtonian flow. Further simulations are also performed here to check the effects of the density and viscosity ratios on the viscoelastic multiphase flows considered in this study. As documented in the Appendix, the results are not very sensitive to a further increase in the density and viscosity ratios beyond $\rho_o/\rho_i = 10$ and $\mu_o/\mu_i = 80$.

4. Results and discussion

Simulations are first performed for a single-phase flow by gradually increasing the Reynolds number from $Re = 10$ to $Re = 1000$. Subsequently, the flow is made more viscoelastic by gradually increasing the Weissenberg number in the range of $1 \leqslant Wi \leqslant 1000$ at a fixed Reynolds number to ascertain whether the flow attains an EIT state without introducing any explicit external perturbations. To facilitate the development of a second normal stress difference (N_2), a square-channel (duct) is used and a small shear-thinning effect is also incorporated by setting $\alpha = 0.001$ for the Giesekus model. A concentrated polymer solution ($\beta = 0.1$) is selected to follow the pathway identified by Samanta *et al.* (2013) for the earlier possible transition to an EIT regime. After identifying the range of Wi for which the single-phase flow remains essentially laminar, bubbles are subsequently injected into fully developed viscoelastic laminar flows at $Wi = 1$, 5 and 10, while keeping Re constant to ascertain whether the presence of bubbles can trigger a flow instability. The bubble volume fraction is kept constant at 3 % for all the cases. The capillary number is fixed at a low value of $Ca = 0.01$ to maintain approximately spherical bubble shapes. The
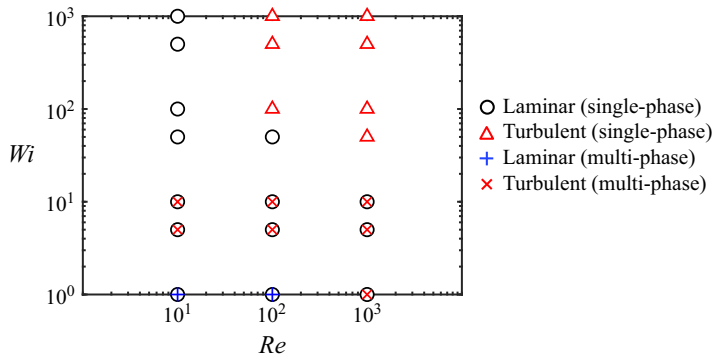
Figure 2. Various flow states in the Re–Wi space ($Ca = 0.01$, $\beta = 0.1$).

resultant single-phase and multiphase flows are presented and discussed in the following sections.

4.1. *EIT in a single-phase flow*

Figure 2 summarises the flow states in the Re–Wi space. At a low value of $Re = 10$, the single-phase flow remains fully laminar for up to $Wi = 1000$. Two points are selected in the computational domain to collect all the components of velocity and viscoelastic stresses at each time step to monitor their evolution to ascertain the attainment of a statistically steady-state solution. One of the 'numerical probes' is located at the centre of the channel ($x^* = 1$, $y^* = 6$, $z^* = 1$), while the other one at 25 % distance ($x^* = 0.5$, $y^* = 6$, $z^* = 1$) from one of the walls. Once the flow reaches a statistically steady state, the simulations are continued at least for another 3λ time units, during which, full flow fields are stored for a further statistical analysis.

The simulations are then repeated for $Re = 100$. While gradually increasing Wi, it is observed that the flow remains laminar until $Wi = 100$. However, for $Wi \geqslant 100$, instabilities start to appear in this low-Re flow. These instabilities start to grow with time and fluctuations are observed ultimately in all three components of velocity akin to a typical turbulent signal. Viscoelastic stresses also start to fluctuate in the time domain, as collected by the numerical probes at two different locations of the channel. It is important to emphasise that no explicit perturbations are provided from outside the system to initialise any instabilities in the flow. Only for $Wi \geqslant 100$, the viscoelastic stresses are high enough to trigger an instability that ultimately leads to a chaotic flow regime. As the flow rate is kept constant for a fixed Re, a sudden increase in the applied pressure gradient is also observed once the flow is transitioned from laminar to this chaotic state, indicating a rapid increase in the drag. The characteristics of this chaotic flow regime for $Wi \geqslant 100$ will be discussed in detail in the subsequent paragraphs.

When Re is increased further to 1000, the transition to a chaotic flow regime starts to appear at a lower value of $Wi \geqslant 50$. This Re is still smaller than the minimum $Re_{cr} \approx 1100$ required for sustaining the inertial turbulence in a channel flow (Owolabi *et al.* 2016). As Wi is increased further, the turbulent intensity of this chaotic regime increases with a change in statistical quantities as well.

Figure 3(*a*) shows the velocity vectors in a vertical cutting xz-plane of the viscoelastic duct flow once it reaches a statistically steady state for the $Re = 1000$ and $Wi = 1000$ case. The instantaneous and time-averaged flow fields are plotted in the left and right panels of figure 3(*a*), respectively. As seen, the instantaneous flow field exhibits a chaotic flow
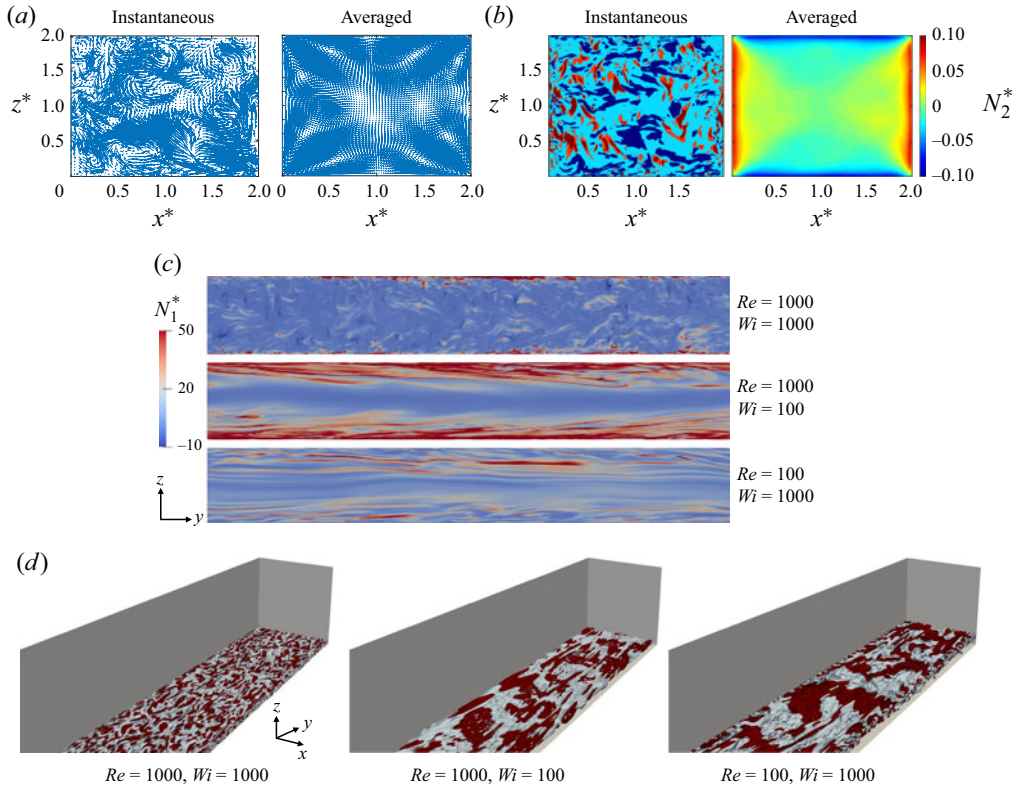
Figure 3. (*a*) Instantaneous (left) and averaged (right) snapshots of velocity vectors showing the secondary flow field at $Re = 1000$ and $Wi = 1000$. (*b*) Instantaneous (left) and time-averaged (right) snapshots of second normal stress difference (N_2) at $Re = 1000$ and $Wi = 1000$. (*c*) Contours of first normal stress difference (N_1) are shown in a statistically steady EIT regime for different values of Re and Wi. (*d*) Iso-surfaces of Q-criterion are shown close to the bottom wall of the channel in a statistically steady EIT regime for different values of Re and Wi. The red and grey colours represent the positive and the negative values, respectively. The contours are plotted at ± 5, ± 0.05 and ± 0.005 for the $(Re, Wi) = (1000, 1000)$, $(1000, 100)$ and $(100, 1000)$ cases, respectively.

regime, while the time-averaged velocity field shows an almost similar secondary flow pattern as also observed in the viscoelastic laminar duct flow with the shear-thinning effect (Li, McKinley & Ardekani 2015; Naseer *et al.* 2024). This secondary flow field is developed in the duct flow primarily due to the presence of a second normal stress difference $N_2 = \bar{\tau}_{zz} - \bar{\tau}_{xx}$. The instantaneous and time-averaged contour plots of N_2 are shown in the left and right panels of figure 3(*b*), respectively. The instantaneous plot confirms the chaotic flow pattern, while the time-averaged one resembles the typical distribution of N_2 in a laminar duct flow. As the EIT regime is associated with long-elongated sheets of the first normal difference (N_1), the distribution of N_1 is also shown in figure 3(*c*) in the yz-plane at the centre of the duct for the various combinations of Re and Wi for which the single-phase flow becomes chaotic. Dubief *et al.* (2023) categorised different EIT regimes based on the structures of N_1 for a 2-D channel flow. For a low value of $Re = 100$, a similar 'chaotic regime' is observed in the present 3-D duct flow as shown in figure 3(*c*). At a higher value of $Re = 1000$, but with a moderate value of $Wi = 100$, this regime is shifted to 'chaotic arrowhead' and once the Weissenberg number is increased to a very high value of $Wi = 1000$, the long-elongated sheets of N_1 break down completely
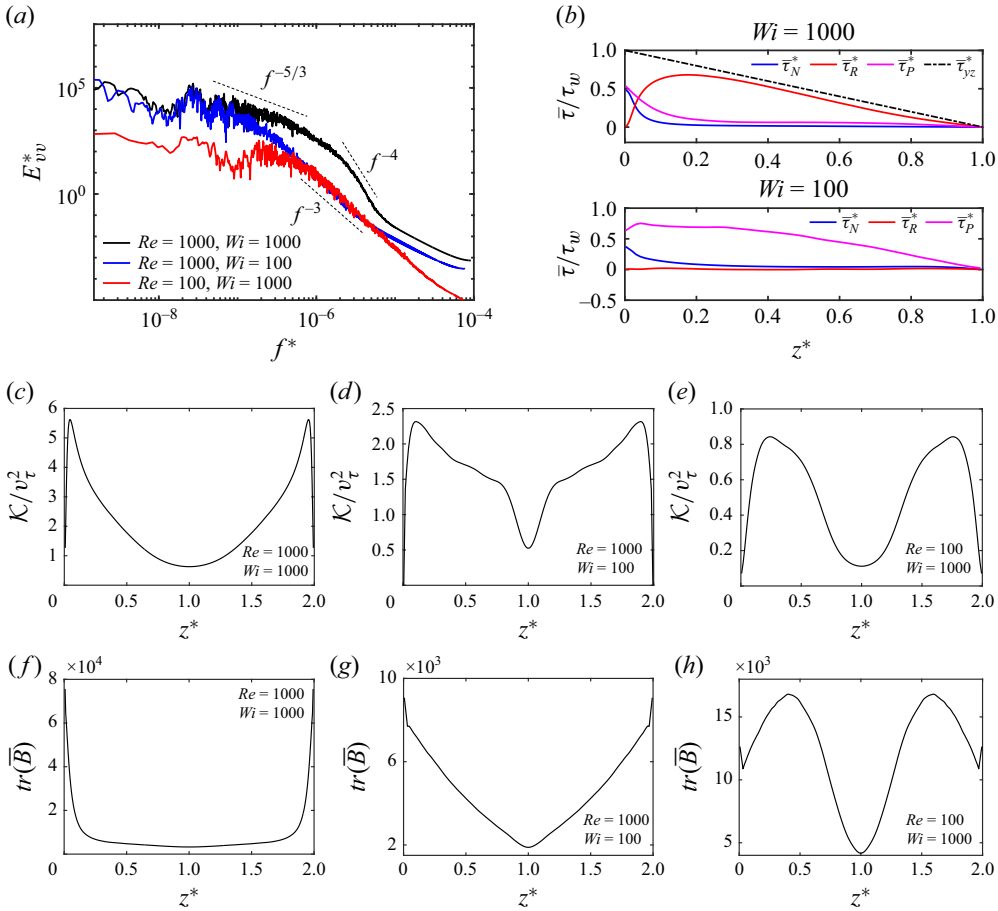
Figure 4. (*a*) One-dimensional energy spectrum for the $(Re, Wi) = (1000, 1000)$, $(1000, 100)$ and $(100, 1000)$ cases. (*b*) Distribution of the components of the average shear stress from the channel wall towards the centre in the mid-plane for $(Re, Wi) = (1000, 1000)$ (top panel) and $(Re, Wi) = (1000, 100)$ (bottom panel). (*c, d, e*) Distribution of turbulent kinetic energy in the mid-plane of the channel for different values of Re and Wi. (*f, g, h*) Average elongation of polymer molecules represented by $tr(\bar{B})$ shown in the same mid-plane.

and the flow starts to resemble a typical inertial turbulence. The iso-surfaces of the second invariant of the velocity gradient tensor (Q-criterion) is depicted in figure 3(*d*) to show the corresponding change in the near-wall vortices for the same combinations of Re and Wi. At a very high value of Re and Wi, the positive and negative contours of the Q-criterion show a chaotic pattern near the wall. With decreasing Re or Wi, the spanwise elongated pattern of positive and negative contours of the Q-criterion starts to appear indicating that the signatures of elastic turbulence become increasingly more apparent in the EIT regime once the elastic effects dominate over the inertial effects. In the absence of any perturbations from outside the system, the flow is laminar at a lower value of Wi in the present scenario, as shown in figure 2. Therefore, a clear pattern of alternating contours of Q-criterion is not visible here, as also observed by Dubief *et al.* (2023).

Figure 4 shows various quantities used to evaluate turbulent characteristics of this single-phase chaotic flow regime for various combinations of Re and Wi. The first one is the 1-D energy spectrum (figure 4*a*). The energy axis is normalised by $(1/2)\rho_o u_o^2$ and the frequency axis by u_o/h. At the higher values of $(Re, Wi) = (1000, 1000)$, the kinetic

energy spectrum shows a typical $-5/3$ scaling at the large scales but it shifts to -4 at the smaller scales (dissipation range). These values are consistent with the results obtained in a single-phase channel flow at lower values of Re by Mukherjee *et al.* (2023) and Foggi Rota *et al.* (2024). The elasticity number, $El = Wi/Re$, provides a measure of the relative strength of elastic to inertial effects. At $(Re, Wi) = (1000, 1000)$, $El = 1$, indicating a balanced elasto-inertial regime. The transition to a -4 slope at smaller scales indicates that viscoelastic effects become significant as the length scale decreases. The steep slope suggests strong suppression of small-scale fluctuations due to elastic stresses in this highly concentrated polymer solution ($\beta = 0.1$). At large scales, the flow behaves like classical turbulence, driven by inertial forces, as seen in figure 3(*c*). At smaller scales, high Wi and low β cause elastic stresses to dominate, altering the cascade. This dual scaling suggests a cross-over frequency where the flow transitions from inertia-dominated to elasticity-dominated dynamics. The exact frequency depends on the balance among Re, Wi and the polymer properties. Once Wi is decreased to $Wi = 100$ while keeping $Re = 1000$, the scaling of energy spectrum shifts from -4 to -3 across the majority of the spectrum (figure 4*a*). It indicates that lowering Wi reduces the elastic effects, allowing inertial forces to distribute energy more effectively to smaller scales, thus resulting in a less steep spectrum. The -3 slope also suggests a transitional EIT regime where the inertial and the elastic effects are not so balanced ($El = 0.1$), with less suppression of small-scale fluctuations compared with the -4 slope at $Wi = 1000$. This is characterised by the 'chaotic arrowhead' regime in figure 3(*c*). Once Re is reduced to 100 while keeping $Wi = 1000$, the energy spectrum again yields a slope of -3. Here, low Re weakens the inertial effects, increasing the relative importance of viscous and elastic forces ($El = 10$). The -3 slope suggests a regime closer to ET, where elastic instabilities drive the flow, modulated by viscous dissipation. The similarity in the -3 slope between $(Re, Wi) = (1000, 100)$ and $(Re, Wi) = (100, 1000)$ indicates that different combinations of inertial and elastic effects can produce similar spectral characteristics. It can be inferred from these scales that once the turbulent flow is entirely governed by inertia (classical inertial turbulence), the energy spectrum assumes a slope of $-5/3$, whereas once the turbulent regime is dominated by the elastic effects with negligible inertia, as in ET, the spectrum exhibits a slope of -4. Any combination of Re and Wi in between these two regimes assumes a slope in between these two limits.

The total mean shear stress in the mid-plane comprises three components: the viscous shear due to mean flow $\bar{\tau}_N$, the Reynolds stress due to velocity fluctuations $\bar{\tau}_R$ and a polymeric stress $\bar{\tau}_P$. Once the flow reaches a statistically steady state, the applied pressure gradient must balance the total shear stress at the four walls of the channel. The three components of shear stress ($\bar{\tau}_N = \mu_o(\partial \bar{v}/\partial z)$, $\bar{\tau}_R = -\rho_o \overline{v'w'}$, $\bar{\tau}_P = \bar{\tau}_{yz}$) are plotted for the central plane of the duct ($x^* = 1$) for two values of $Wi = 1000$ and $Wi = 100$ at $Re = 1000$ (figure 4*b*). The fluctuating and the time-averaged quantities are denoted by prime ($.'$) and overbar ($\bar{.}$), respectively. Note that the averaging is performed both in time and in streamwise direction since the flow is expected to be homogeneous in the streamwise direction once a statistically steady state is reached. The stress components are normalised by the local shear stress at the wall of the respective plane. For the high value of $Wi = 1000$, it is observed that the stress balance in the mid-plane of the channel resembles that of a classical inertial turbulence. The viscous stress is maximum at the wall and decays to zero at the channel centre, whereas the Reynolds stress is zero at the wall, gradually increases to its peak value and then goes to zero at the channel centre. The viscoelastic stress also follows the viscous stress profile, and becomes maximum at the wall and zero at the channel centre. As a result, the total shear stress decays linearly from the wall towards

the channel centre (figure 4*b*). Once *Wi* is reduced to 100 while keeping $Re = 1000$, the magnitude of Reynolds stress becomes negligibly small compared with viscous and polymeric stresses. Although the -3 scaling of the energy spectrum and the turbulent signal are indicative of a turbulent flow field at this comparatively lower value of $Wi = 100$, the Reynolds stress becomes negligibly small compared with the overall shear stress in the mid-plane. These not-so-smooth profiles of different shear stress components indicate a clear departure of the turbulent flow field from the inertial one. The distribution of the turbulent kinetic energy (TKE) $\mathcal{K} = 0.5(\overline{u'^2} + \overline{v'^2} + \overline{w'^2})$ is shown in figures 4(*c*), 4(*d*) and 4(*e*) at the mid-plane where TKE is found to be maximum near the walls and decays to a minimum value at the centre. Interestingly, the average elongation of polymer molecules quantified by the trace of the conformation tensor $tr(\bar{B})$ shows a similar trend for different values of *Wi*, as shown in figures 4(*f*), 4(*g*) and 4(*h*). It is worth mentioning that the value of the applied pressure gradient decreases as *Wi* increases for a constant value of *Re*, indicating a decrease in the drag force. As the chaotic flow is driven by elasticity, this unexpected drag reduction with an increase in *Wi* is attributed to the shear-thinning effect that dominates the drag increase caused by the pronounced chaotic flow.

Garg *et al.* (2018) have shown that for the large Weissenberg numbers, the viscoelastic pipe flow can be linearly unstable to axisymmetric disturbances down to a critical Reynolds number of $Re_{cr} \approx 63$. Wan, Sun & Zhang (2021) and Buza, Page & Kerswell (2022) later demonstrated that the polymer concentration (β) is the main controlling factor. At a higher polymer concentration, the unstable region shrinks and the transition is mostly supercritical. A similar mechanism seems to be at play in the present single-phase duct flow, where transition occurs even in the absence of any finite perturbation at a high Weissenberg number. The subcritical transition does not occur in a single-phase flow due to the stabilising role of high polymer concentration ($\beta = 0.1$), as seen for the lower Weissenberg number cases for all the three Reynolds numbers.

Foggi Rota *et al.* (2024) have demonstrated that a single-phase viscoelastic flow can sustain a chaotic flow state in a straight channel at a Reynolds number as low as $Re = 0.5$ (*Wi* = 50) if started from a turbulent initial condition for a dilute polymer solution by using the FENE-P model with $\beta = 0.9$. The value of $Wi = 50$ was kept constant in their simulations while bringing down the Reynolds number from $Re = 2800$ to $Re = 0.5$ to keep the polymers in their stretched state. To observe whether the chaotic state is sustained in the present scenario of a duct flow with a concentrated polymer solution, extensive simulations are next performed by keeping the Reynolds number constant at $Re = 1000$ and the Weissenberg number is reduced from $Wi = 1000$ to [500, 100, 50, 40, 10]. Each of the lower *Wi* is started by using the initial conditions of the previous higher *Wi* case. It is found that the chaotic flow state is sustained until $Wi = 40$. When *Wi* is further reduced to 10, the single-phase flow is laminarised. Next, the same simulations are repeated by fixing the Reynolds number at $Re = 100$. The Weissenberg number is reduced gradually from $Wi = 1000$ until 10 and it is observed that the chaotic flow is sustained until $Wi \geqslant 40$. The same limit of $Wi \geqslant 40$ is observed for the $Re = 10$ cases to sustain a chaotic regime in this duct flow if perturbed initially. It can be concluded that if the flow is perturbed initially, the chaotic flow is sustained in this single-phase viscoelastic duct flow only if the value of $Wi \geqslant 40$. Below this value, the single-phase flow is laminarised. This value is close to $Wi = 50$ used by Foggi Rota *et al.* (2024) in their channel flow simulations.

It is important to highlight that exceptionally high Weissenberg numbers required to trigger flow instability in the absence of any discrete external perturbations in this rectilinear channel may seem impractical. However, it should be noted that *Wi* is defined based on the average flow velocity in the channel. As shear rate decreases significantly towards the

channel centre in this duct flow, the effective local Weissenberg number is actually much lower than the nominal value of *Wi*, which is based on the average flow velocity.

4.1.1. *Turbulent kinetic energy*

The turbulent kinetic energy ($\mathcal{K} = (1/2)\overline{u'_i u'_i}$) in a viscoelastic flow evolves by

$$
\frac{\partial \mathcal{K}}{\partial t} = \overbrace{-\bar{u}_j \frac{\partial \mathcal{K}}{\partial x_j}}^{\mathcal{A}} \overbrace{- \frac{1}{2} \frac{\partial \left(\overline{u'_i u'_i u'_j} \right)}{\partial x_j}}^{\mathcal{Q}} \overbrace{- \frac{1}{\rho_o} \overline{u'_i \frac{\partial p'}{\partial x_i}}}^{\mathcal{R}} \overbrace{- \left(\overline{u'_i u'_j \frac{\partial \bar{u}_i}{\partial x_j}} \right)}^{\mathcal{P}} + \overbrace{\frac{1}{2} \frac{\partial}{\partial x_j} \left(\nu_s \frac{\partial \overline{u'_i u'_i}}{\partial x_j} \right)}^{\mathcal{D}}
$$

$$
\underbrace{- \nu_s \overline{\frac{\partial u'_i}{\partial x_j} \frac{\partial u'_i}{\partial x_j}}}_{\epsilon} + \underbrace{\frac{1}{\rho_o} \left(\overline{u'_i \frac{\partial \tau'_{ij}}{\partial x_j}} \right)}_{\mathcal{W}_p} + \underbrace{\overline{u'_i f'_i}}_{\mathcal{B}}, \tag{4.1}
$$

where $\mathcal{A}, \mathcal{Q}, \mathcal{R}, \mathcal{P}, \mathcal{D}, \epsilon, \mathcal{W}_p$ and $\mathcal{B}$ represent advection by mean flow, transport by velocity fluctuations, transport by pressure, production by mean flow, viscous diffusion, viscous dissipation, polymer work and work done by body force, respectively. In a viscoelastic turbulent flow, $\mathcal{W}_p$ may change its sign and can serve as either dissipation or production depending upon the signs of the polymer stress fluctuations and fluctuating velocity gradients, as has been observed in both experimental (Ptasinski *et al.* 2001) and numerical (Dallas, Vassilicos & Hewitt 2010) works.

To get better insight of the EIT regime in this duct flow, these terms are averaged in time and in the streamwise (y) direction once the flow reaches a statistically steady state. The constant contours of all the terms in (4.1) normalised by v_τ^2 are shown in figure 5 at two different values of *Re* in a vertical cutting xz-plane except for the body force term that is zero for this single-phase flow. For $Re = 1000$, the advection by mean flow (figure 5*a*-left) shows small regions of positive peaks at the four corners and towards the centre of the duct. A pattern of four negative peaks is also observed slightly away from the walls at this high-Reynolds-number EIT flow. However, once the Reynolds number is lowered to $Re = 100$, the magnitude of the advection term becomes negligibly small. Similarly, a symmetric pattern of transport term is observed for the higher Reynolds number (figure 5*b*-left) and the same term becomes negligibly small at lower inertia. At $Re = 1000$, the positive and negative peaks of the transport term remain closer to the channel walls except at the corners where it remains approximately zero. An opposite trend is observed for the pressure term (figure 5*c*). Once the flow is dominated by the inertial effects ($Re = 1000$), the pressure term remains significant while, in an elastically dominated EIT regime ($Re = 100$), it shows a symmetric pattern of positive and negative zones, however, with a negligibly small magnitude. The positive peaks of the pressure term extend from four corners of the duct until the centre with negative peaks in the vicinity of the channel walls. Turbulence production by the mean flow is mainly produced near the walls except at the four corners (figure 5*d*) and becomes zero in most of the central region of the duct with a symmetric pattern at $Re = 1000$. However, in the elastically dominated EIT flow ($Re = 100$), this pattern changes with four regions of positive peaks away from the walls. As the turbulence is mainly produced by the elastic effects at $Re = 100$, the magnitude of the production term also remains negligibly small. The diffusion term (figure 5*e*) shows positive peaks adjacent to the walls except at the corners, immediately followed by the negative peaks before decaying to zero for $Re = 1000$ whereas, for the $Re = 100$ case, it is positive near the walls and remains chaotic in most of the remaining central portions of the duct. The dissipation term shows a similar pattern for both cases
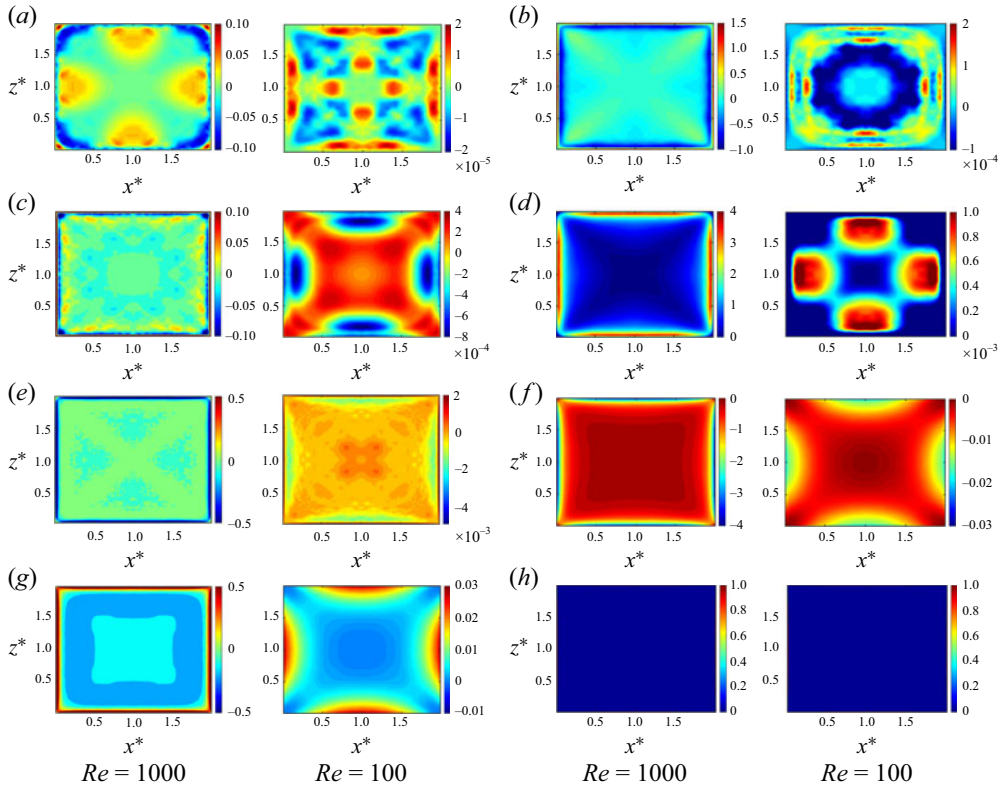
Figure 5. Contours of (*a*) advection by mean flow, (*b*) transport by velocity fluctuations, (*c*) transport by pressure, (*d*) production by mean flow, (*e*) viscous diffusion, (*f*) viscous dissipation, (*g*) polymer work and (*h*) time derivative of TKE are shown in a vertical cutting xz-plane for the (left) $Re = 1000$, $Wi = 1000$ and (right) $Re = 100$, $Wi = 1000$ cases, respectively.

(figure 5*f*), i.e. it is maximum at the walls except in the corners and becomes zero towards the duct centre. The most important term in this EIT regime is the work done by the elastic force (figure 5*g*) as it can contribute towards both generation or dissipation of turbulence. At higher inertia ($Re = 1000$), the positive peak of the polymer work is observed to be closer to the four walls of the channel. It indicates that the viscoelastic stresses contribute to the turbulence production closer to the walls, but act as a dissipating sink away from it. The same term remains negligible at the centre. Interestingly, at lower inertia ($Re = 100$) where the elastic effects dominate, the polymer stresses contribute towards turbulence dissipation at the four corners and towards the central region of the duct. The turbulence production by polymer stresses is concentrated near the walls away from the corners. The viscous dissipation and the pressure terms follow the similar pattern, as seen in figures 5(*f*) and 5(*c*), respectively. Finally, the summation of all the terms in (4.1) approaches zero confirming that a statistically steady state is reached, as shown in figure 5(*h*).

Notably, the distribution of various components of TKE in the present EIT regime of a highly concentrated polymer solution at low Re is markedly different than that in a dilute viscoelastic turbulent duct flow at high Re as studied by Shahmardi et al. (2019), where the turbulent statistics of the flow were entirely dominated by the inertial effects.
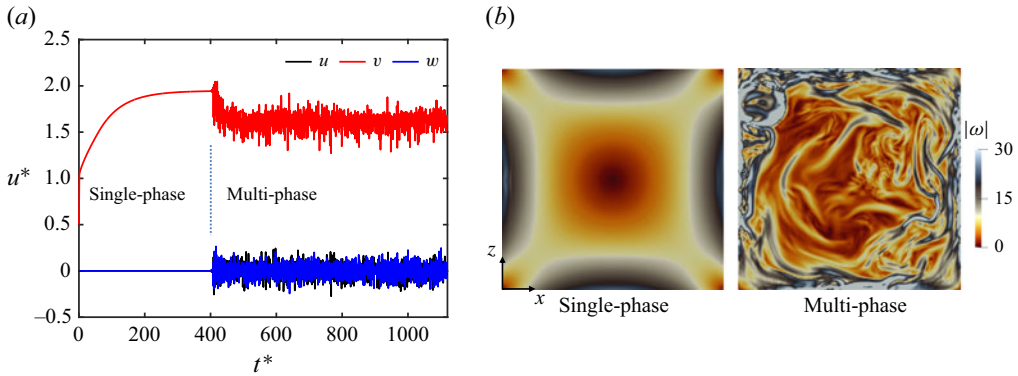
(*a*)

(*b*)

Figure 6. (*a*) Evolution of flow velocity and its transition to turbulent state once bubbles are injected into the flow. (*b*) Contours of vorticity magnitude in an xz-plane at the centre of the domain for the single-phase and multiphase regimes ($Re = 1000$, $Wi = 5$, $\beta = 0.1$, $Ca = 0.01$).

4.2. *EIT in a multiphase flow*

For a given Reynolds number, a significantly high Wi is always required to achieve the EIT state in a single-phase flow in the absence of any external perturbations, as has been shown in the previous section. When Re is low (e.g. $Re = 10$), even a Weissenberg number as high as 1000 cannot make the flow unstable (figure 2). Similarly, the single-phase flow is found to be essentially laminar at the lower values of Wi even when the Reynolds number is as high as $Re = 1000$.

We next examine the effects of bubble injection into the viscoelastic laminar channel flow. For this purpose, simulations are performed for three relatively low values of $Wi = 1$, 5 and 10 at each value of $Re = 10$, 100 and 1000. Note that the single-phase flow remains laminar for these combinations of Wi and Re. Calculations are first carried out for the single-phase flow until a statistically steady state is reached. Then, spherical bubbles are injected instantaneously into the flow with a volume fraction of 3 % and a relative bubble size of $d_b/2h = 0.2$, where d_b is the bubble diameter. The bubbles are initially injected randomly and uniformly in the entire duct. The capillary number is fixed at $Ca = 0.01$ to keep the bubbles nearly spherical. The state of this multiphase flow field is continuously monitored at each time step using the two numerical probes as for the single-phase case. By introducing the bubbles into the flow, the flow is found to achieve a chaotic state even for Reynolds and Weissenberg numbers as low as $Re = 10$ and $Wi = 5$. Time histories of instantaneous velocity components are plotted in figure 6(*a*) for the $Re = 1000$ and $Wi = 5$ case to show the transition from a laminar to an EIT state after the injection of bubbles. Bubbles are injected at approximately $t^* = 400$. As seen, the signals are very smooth until the injection of bubbles indicating a laminar flow. Once the bubbles are injected into the flow, all three components of the velocity exhibit random fluctuations indicating a transition to the EIT state. These fluctuations propagate throughout the domain over time, ultimately leading to a fully chaotic flow field. This chaotic flow state is visualised by plotting constant contours of vorticity ($\boldsymbol{\omega} = \nabla \times \boldsymbol{u}$) magnitude in figure 6(*b*) for the single-phase and multiphase regimes in a vertical cutting xz-plane at the centre of the duct. Once the flow reaches a statistically steady state after the injection of bubbles, the simulations are continued at least for another 10 flow-through time units ($10 \times 12h/u_o$) to collect data for further statistical analysis.

Although not shown here due to space considerations, further simulations are performed to demonstrate the effect of bubble-induced streamline curvature on the destabilisation of

the flow. For this purpose, simulations start from a two-phase Newtonian laminar flow at $Re = 100$. Subsequently, the flow is made weakly viscoelastic by setting a small value of $Wi = 0.5$ and the simulation is continued until the viscoelastic stresses are fully developed and no flow destabilisation is observed. Then, the Weissenberg number is gradually increased first to $Wi = 1$, then to $Wi = 2$ and eventually to $Wi = 5$, while the flow state is continuously monitored. In this process, the simulations are carried out until a statistically steady state is reached before increasing Wi in each step. No transition occurred at low Wi, i.e. $Wi \leqslant 2$. The flow remained laminar despite the presence of bubbles, confirming that the initial discontinuity (bubble injection) alone is insufficient to trigger transition to turbulence. Transition is finally observed at $Wi = 5$. The transition is governed by the interplay of elasticity and streamline curvature but not the transient discontinuity. The destabilisation coincided with the development of strong streamline curvature around bubbles, consistent with prior studies showing that viscoelastic stresses amplify curvature-driven instabilities, as first observed and quantified by McKinley, Pakdel & Öztekin (1996) and has also been confirmed in our earlier work as well (Naseer *et al.* 2024).

Figure 7(*a*) shows the distribution of first normal stress difference (N_1) in the mid-plane for three different values of $Re = 10$, $Re = 100$ and $Re = 1000$ at $Wi = 10$. A 'chaotic arrowhead' regime is observed for all three values of Re at this relatively low Wi for which the single-phase flow remains fully laminar. Note that all bubbles are of the same size in figure 7(*a*) and the seemingly different appearance of the bubble sizes is simply caused by the out-of-plane bubbles at this particular time instant. The constant contours of Q-criterion at the walls for the same three cases are depicted in figure 7(*b*), showing a chaotic pattern similar to that observed in the single-phase cases at a low value of Wi (figure 3*d*). The contours of Q-criterion at the wall are shown in figure 7(*c*) for $Re = 10$, 100 and 1000 at $Wi = 1$. It is observed that, for this low $Wi = 1$ case, the flow remains laminar at the walls for the $Re = 10$ and $Re = 100$ cases. Small perturbations remain confined to the immediate surroundings of bubbles. The positive and negative structures of Q-criterion are only visible at the walls once plotted at negligibly smaller values (i.e. $\pm 1 \times 10^{-5}$). For $Re = 1000$, however, a chaotic flow regime is observed even at $Wi = 1$ as seen by the contours of Q-criterion (figure 7*c*).

The bubble distributions in the duct are depicted in figure 7(*d*). It is interesting to see that, although the bubble distribution is essentially uniform in the other cases, the majority of the bubbles are aligned in the centre of the duct forming a string-shaped pattern for the lower values of $Re = 10$ and $Wi = 1$, which also explains the reason why the disturbances remain confined to the core region of the duct away from the walls for this case. In the case of non-colloidal spherical solid particles, Won & Kim (2004) have experimentally shown that although the main driving force for the lateral migration of particles is the first normal stress difference, particle alignment is actually promoted by the shear-thinning effect for a particular rheological setting. In the present case of bubbles, the role of shear-thinning effect in the alignment of bubbles is investigated by performing another simulation at $Re = 10$ and $Wi = 1$ with a higher shear thinning and the results are shown in figure 8. The change in the effective viscosity (μ_e) of the flow due to the shear-thinning effect at different shear rates ($\dot{\gamma}$) is governed by the concentration of polymers (β) and the mobility factor (α) in the Giesekus model. The slope of viscosity versus shear rate plot is controlled by the mobility factor α and the final value of viscosity at a high enough shear rate is determined by the concentration of polymers β (Yoo & Choi 1989). The vertical line in figure 8(*a*) indicates the shear rate at the wall for the mid-plane of the duct for the $Re = 10$ and $Wi = 1$ case. Once the mobility factor is increased to $\alpha = 0.1$, a random distribution of bubbles is observed instead of the string-shaped aggregation at the centre of the duct (figure 8*b*). We thus conclude that, unlike the solid particles, a
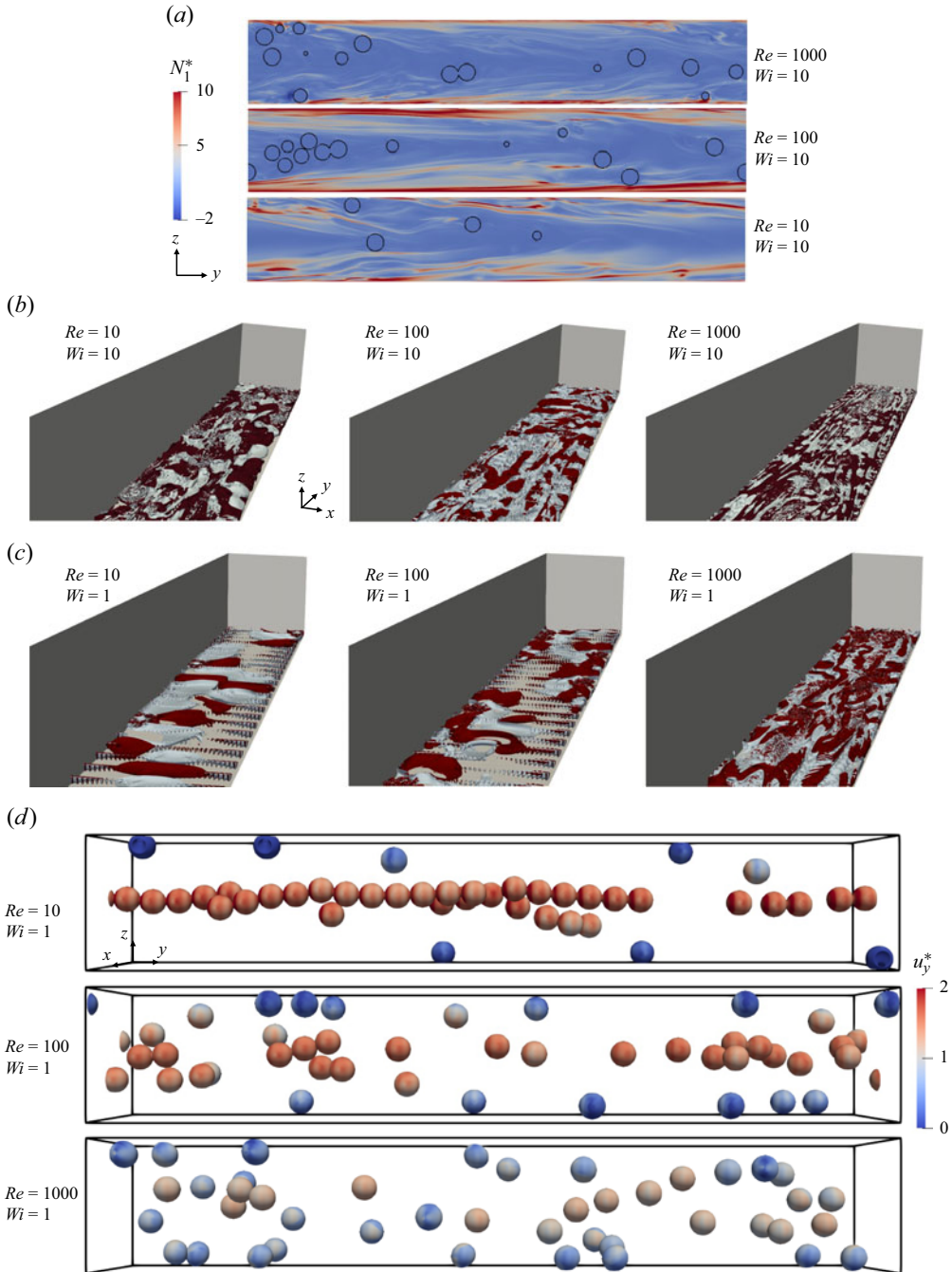
Figure 7. (*a*) Contours of N_1 in the mid-plane for different values of Re at $Wi = 10$. Iso-surfaces of Q-criterion at the bottom walls of the channel for the multiphase EIT regime at (*b*) $Wi = 10$ and at (*c*) $Wi = 1$ for different values of Re. For panel (*b*), the contours are plotted at ± 0.00001, ± 0.001 and ± 0.01 for the $Re = 10$, 100 and 1000 cases with red colour (positive) and grey (negative), respectively. For panel (*c*), the contours are plotted at ± 0.00001 for $Re = 10$, 100 and at ± 0.1 for the $Re = 1000$ case. (*d*) Distribution of bubbles coloured by the magnitude of streamwise flow velocity in the channel for different values of Re at $Wi = 1$.
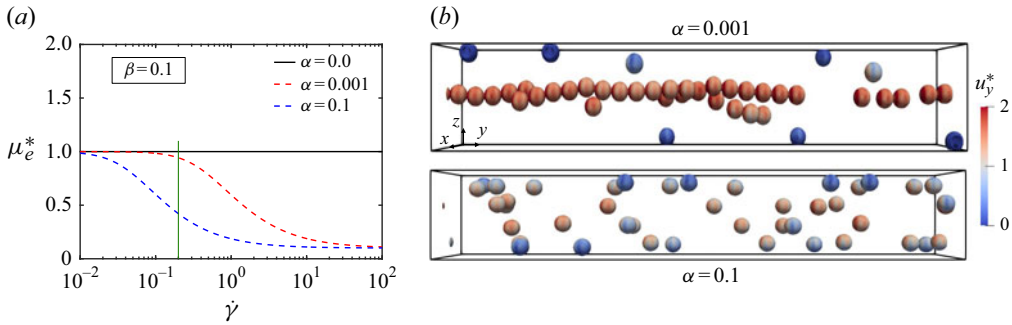
Figure 8. (*a*) Change in the effective viscosity of a Giesekus fluid in a concentrated polymer solution. The vertical line shows the value of shear rate at the wall for the central yz-plane of the present duct flow. (*b*) Distribution of bubbles in the duct for different values of shear-thinning parameter α ($Re = 10$, $Wi = 1$, $Ca = 0.01$, $\beta = 0.1$).

higher shear-thinning effect of the ambient fluid breaks up the alignment of bubbles at least for this particular rheological setting. Further investigation is required to reveal the exact mechanism behind the role of the shear-thinning effect on different forces acting on the bubbles and causing them to align in the central region of the duct.

Figure 9(*a*) shows that, for the case of $(Re, Wi) = (10, 1)$, the majority of bubbles accumulate in the core region, and the perturbations remain confined to immediate surroundings of the bubbles indicating a laminar flow, as shown by the contours of Q-criterion. When the inertia is increased ($Re = 100$) at the same low value of $Wi = 1$, the bubbles become more uniformly distributed, but the flow still remains laminar. Finally, once the inertia is sufficiently high ($Re = 1000$), the bubbles become randomly distributed in the entire duct and a fully chaotic flow regime is observed in the entire domain (figure 9*a*) with a significant increase in the friction drag. Figure 9(*b*) shows a 1-D energy spectrum of the streamwise component of flow velocity for $Wi = 1$, $Wi = 5$ and $Wi = 10$ at $Re = 10$. Once the flow reaches a statistically steady state, the velocity signal is collected from the point away from the centre ($x^* = 0.5$, $y^* = 6$, $z^* = 1$) to avoid the noise due to the bubble cluster. The flow velocity inside the bubbles is filtered out from the signal. A slope of -2 is observed for the $Wi = 5$ and 10 cases when the flow is chaotic in the entire domain. This slope is the same as the temporal spectrum scaling of centreline velocity observed by Lellep, Linkmann & Morozov (2024) indicating a similar chaotic state. The energy spectra of the $Wi = 5$ and $Wi = 10$ cases overlap each other, showing a similar flow state for both the cases in the presence of bubbles. As the flow is not fully chaotic at $Wi = 1$ and its signal shows a very high intermittency, the same is manifested in its spectrum where the slope does not match with the slopes of the $Wi = 5$ and 10 cases. For the $Re = 100$ cases, the slope for $Wi = 1$ gets closer to the slopes in the $Wi = 5$ and 10 cases, and finally at $Re = 1000$, all the three cases show a similar slope of -2 (figure 9*d*). This slope of -2 is greater than the classical slope of $-5/3$ in the inertial turbulence, but still less than -4 reported for a purely elastic turbulence in the absence of inertia (Datta *et al.* 2022) or at a very high value of $Wi = 1000$ observed in the single-phase cases (figure 4*a*, *c*). As this multiphase EIT regime is achieved at the lower values of Wi, it is governed by both inertia and viscoelasticity, and hence the slope remains in between these two limits.

The distribution of different components of shear stress from the channel wall towards the centre are shown in figures 9(*e*), 9(*f*) and 9(*g*) in the mid-plane of the duct for $Re = 10$, 100 and 1000 cases, respectively. As the flow is multiphase, an additional contribution from the surface tension force of the bubbles ($\bar{\tau}_S$) is added towards the total shear stress
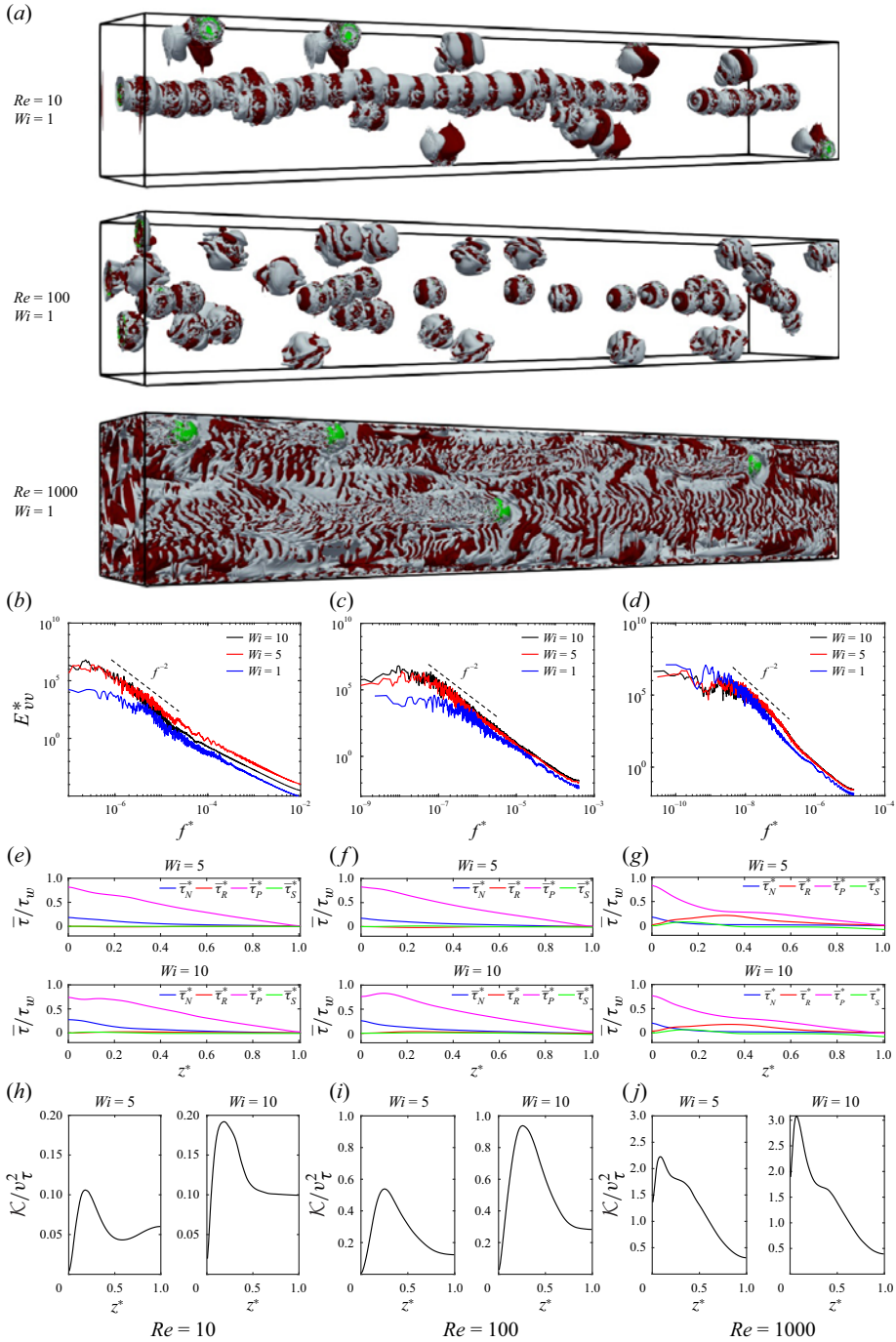
Figure 9. (*a*) Iso-surfaces of *Q*-criterion are shown at different values of *Re* for *Wi* = 1. The contours are plotted at ±0.002, ±0.2 and ±2 for the *Re* = 10, 100 and 1000 cases, respectively. The bubbles are marked with green colour, while the positive and negative values of *Q*-criterion are marked with red and grey colours, respectively. (*b, c, d*) One-dimensional energy spectrum, (*e, f, g*) the distribution of various components of shear stress and (*h, i, j*) turbulent kinetic energy (𝒦) are plotted in the mid-plane for the *Re* = 10 (left), *Re* = 100 (middle) and *Re* = 1000 (right) cases, respectively (*β* = 0.1 and *Ca* = 0.01).

balance. However, this contribution remains much smaller than the remaining components as the bubble volume fraction is a mere 3 %. Similar to the single-phase flow cases, these stress components are normalised by the local shear stress at the wall of the mid-plane. As seen in the figure, the chaotic flow regime is dominated by the viscoelastic stress ($\bar{\tau}_P$) followed by the viscous stress due to the mean flow ($\bar{\tau}_N$). These two stress components are highest at the wall and decay to zero towards the channel centre where the shear rate is minimum. The contribution of the Reynolds stress ($\bar{\tau}_R$) remains negligible for the $Re = 10$ and $Re = 100$ cases. The Reynolds stress component $\bar{\tau}_R$ starts to show its effect once the inertia becomes high enough in the $Re = 1000$ cases. As the source of flow instability is the curved streamlines around the bubble in this multiphase flow regime (McKinley *et al.* 1996), the transition to the EIT state greatly depends upon the distribution of bubbles across the channel. The role of viscoelasticity in promoting the bubble migration towards the channel centre or towards the wall is governed by the relative change in the convective time scale of the bubbles and the polymer relaxation time, as has been explained by Bothe *et al.* (2022). A similar observation was also made in our earlier work (Naseer *et al.* 2024). The distribution of turbulent kinetic energy (TKE) for all these three values of Re shows a peak value near the wall and minimum at the channel centre, as shown in figures 9(*h*), 9(*i*) and 9(*j*). By increasing the value of *Wi*, the magnitude of TKE also increases following the same qualitative trend in agreement with our previous study of viscoelastic turbulent single phase case (Izbassarov *et al.* 2021*b*).

Next, further simulations are performed to examine the effects of size and number of bubbles on the transition and resulting chaotic flow for the $(Re, Wi) = (1000, 1)$ case. First, the number of bubbles are increased from the previous volume fraction of $\Phi = 3\%$ to $\Phi = 9\%$ while keeping the bubble size the same, and then the bubble volume is decreased by 50 % while keeping the volume fraction the same at $\Phi = 3\%$. As shown in figure 10, neither the number of bubbles nor their size has any significant effect on the scaling of energy spectrum except for a slight increase in the energy content at the smaller scales for $\Phi = 9\%$. Moreover, no significant change in transition to a chaotic state is observed by varying the number of bubbles or their size.

Once the flow reaches a steady state, the applied pressure gradient is balanced by the total shear stress at the walls and the average wall shear stress can be simply computed as $\bar{\tau}_w = -(h/2)(\mathrm{d}p_o/\mathrm{d}y)$. The change in the drag is quantified by $\Delta D = (\bar{\tau}_w - \tau_{w_o})/\tau_{w_o}$, where τ_{w_o} is the wall shear stress of the corresponding Newtonian laminar flow for the same Reynolds number. Figure 11 summarises the percentage change in drag for all the multiphase simulations. The single-phase viscoelastic laminar flow has lower drag as compared with the Newtonian laminar flow for the same value of Re. Understandably, as the inertia increases in this shear thinning viscoelastic fluid once the flow is made viscoelastic, the drag is reduced. For a particular value of *Wi*, the percentage reduction in drag is found to be the same for every value of Re. However, the drag increases significantly once a viscoelastic flow transitions to a chaotic turbulent state after injecting the bubbles (figure 11). In particular, a rapid increase in the drag is observed at $Re = 1000$ once the flow becomes turbulent for all three values of *Wi*. It is interesting to observe that, although the drag increases for the $Re = 10$ and 100 cases at $Wi = 5$ and 10 upon transition to the EIT state, it still remains less than that of the respective Newtonian laminar state. Another interesting feature is also observed at $Wi = 1$ for the $Re = 10$ and 100 cases. Once bubbles are injected into the flow, minor fluctuations remain confined to the core region away from the walls where the bubbles collect and form a string-shaped pattern ($Re = 10$) or small clusters ($Re = 100$). The flow remains essentially laminar closer to walls and in the major portion of the duct. In this regime, the drag is reduced as compared with the single-phase laminar state. For this case, the bubbles forming a string-shaped
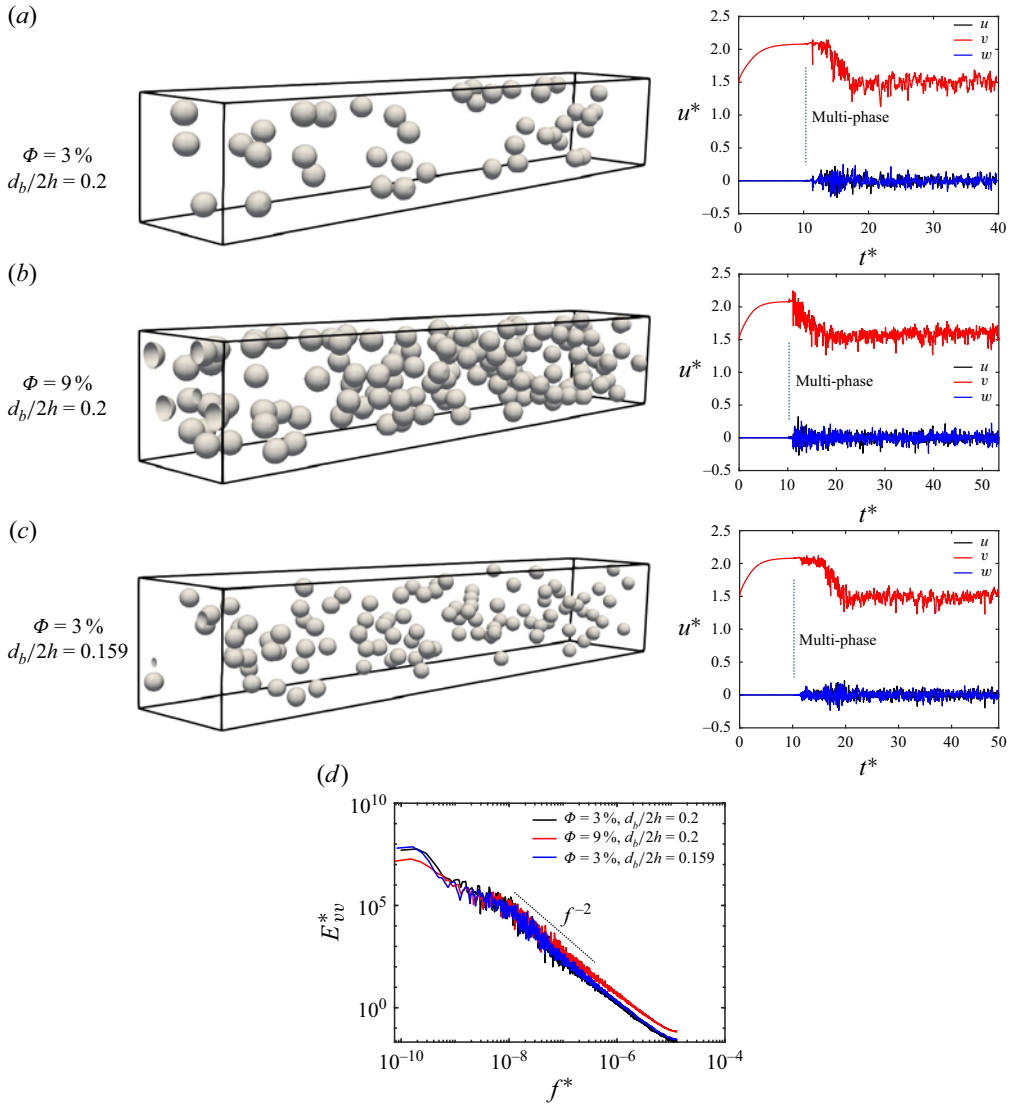
Figure 10. Effects of number of bubbles and bubble size. The bubble distribution (left) and the evolution of flow velocity (right) for the void fraction of (*a*) $\Phi = 3\,\%$, (*b*) $\Phi = 9\,\%$ for the same bubble size of $d_b/2h = 0.2$ and (*c*) for the bubble size of $d_b/2h = 0.2/\sqrt[3]{2} = 0.159$ with $\Phi = 3\,\%$. (*d*) One-dimensional energy spectra for the same cases ($Re = 1000$, $Wi = 1$, $Ca = 0.01$, $\alpha = 0.001$).

pattern create a low viscosity corridor at the core region where they move faster and thus the streamwise component of flow velocity is slightly increased. As a result, the applied pressure gradient is reduced effectively to maintain the same flow rate. Furthermore, it is important to highlight that the magnitude of drag is small for this laminar flow, so the change is also small. At a higher inertia ($Re = 1000$), the flow becomes fully chaotic in the entire channel, and thus the drag is increased significantly even for the $Wi = 1$ case (figure 11).

It is interesting to note that for the (Re, Wi) = (10, 10) and (100, 10) cases, the flow has become completely chaotic and the EIT state is achieved by injecting the bubbles into the
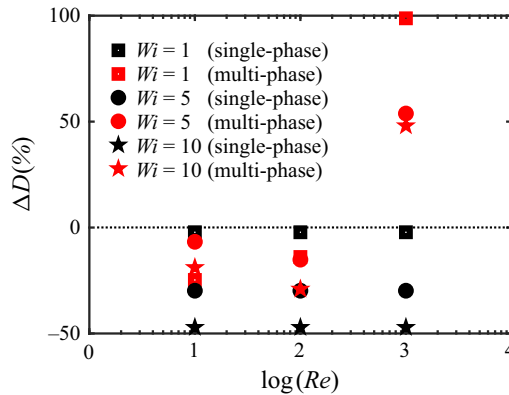
Figure 11. Percentage change in drag measured by the change in total shear stress at the wall ($\overline{\tau}_w$) as compared with the Newtonian laminar flow once the flow is made viscoelastic and is subsequently transitioned to turbulent state by injecting the bubbles.

flow; however, the drag is still less than the corresponding Newtonian laminar state, which is primarily attributed to the shear-thinning effect of viscoelastic fluid (figure 11).

4.2.1. *TKE in a multiphase EIT regime*

To get further insight into the multiphase EIT regime, all the terms in (4.1) are integrated in the streamwise direction and averaged in time after the flow reaches a statistically steady state. The results are plotted in figure 12 for $Re = 100$ and $Re = 1000$ at $Wi = 10$. Compared with the single-phase case shown in figure 5, a prominent effect of bubbles at low Weissenberg number is observed in smoothing sharp gradients near the wall in all the terms that contribute to TKE. We note, however, that comparison between single-phase and multiphase cases should be interpreted only qualitatively since Wi is two orders of magnitude higher in the single-phase case. Figure 12 shows that the magnitudes of all terms are amplified as Re is increased from 100 to 1000, but the amplification is more pronounced in advection ($\mathcal{A}$), turbulent transport ($\mathcal{Q}$), production by mean flow ($\mathcal{P}$) and viscous diffusion ($\mathcal{D}$) terms. There are also some qualitative differences in these terms in the $Re = 100$ and $Re = 1000$ cases. The peak values of $\mathcal{A}$, $\mathcal{Q}$, P and ϵ occur in the corners and in the middle of the side walls for $Re = 100$ and $Re = 1000$, respectively. In contrast to the single-phase case, the maximum value of $\mathcal{R}$ occurs in the central portion of the duct due to the presence of bubbles (figure 12*c*). Significant viscous dissipation observed in the channel centre is also attributed to the presence of bubbles there. The positive peaks of polymer work for the multiphase case shows that it still contributes towards the production instead of dissipation in some portions of the domain (figure 12*g*). The body force term contributes significantly to the TKE budget now due to the work done by the surface tension (figure 12*h*).

Notably, the chaotic flow state at these lower values of Weissenberg numbers is only sustained in the presence of bubbles. If the bubbles are removed, the single-phase flow would laminarise, as observed in the simulations of single-phase flow where the chaotic flow state could not be sustained below $Wi \leqslant 40$.

In the ET regime (very low Re), it is well established that a sufficiently strong extensional perturbation is required to destabilise the flow and trigger chaos. As inertia increases, the threshold for instability decreases and the flow becomes more susceptible to a wider range of perturbations – including those introduced by bubbles. In the present simulations, the presence of bubbles provides persistent, finite-amplitude disturbances that
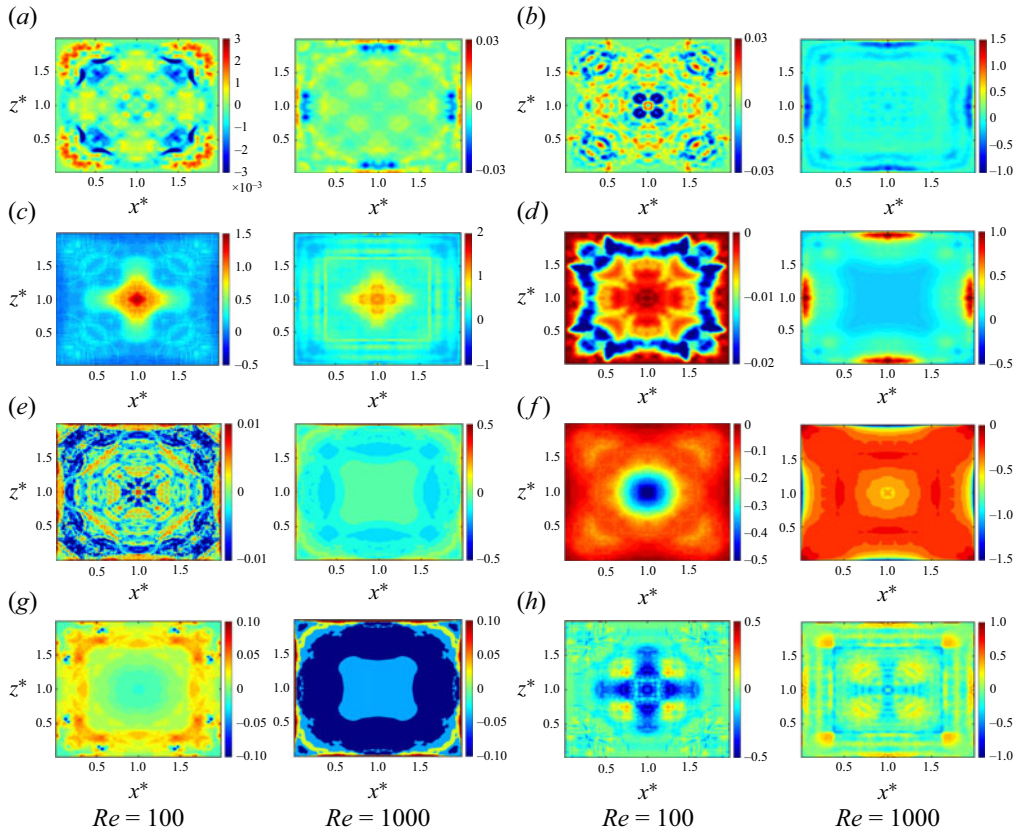
1020 A20-21

Figure 12. Contours of (*a*) advection by mean flow, (*b*) transport by velocity fluctuations, (*c*) transport by pressure, (*d*) production by mean flow, (*e*) viscous diffusion, (*f*) viscous dissipation, (*g*) polymer work and (*h*) body force terms are shown in a vertical cutting xz-plane for (left) $Re = 100$, $Wi = 10$ and (right) $Re = 1000$, $Wi = 10$ multiphase cases, respectively.

can maintain a chaotic state even as inertia becomes more significant. Thus, the bubbly chaotic state observed in the present study at moderate Re can be interpreted as a form of ET that is transitioning towards EIT as inertia increases. This is further supported by the fact that the energy spectra do not yet reach the inertial $-5/3$ scaling, and the flow structures retain characteristic features of ET.

In summary, ET and EIT can be seen as two ends of a spectrum, with present results occupying an intermediate and transitional regime. The bubbly chaotic state in the present scenario likely represents a version of ET influenced by finite inertia and persistent multiphase perturbations, rather than a fully developed EIT state. The spectra and flow localisation support this interpretation.

5. Conclusions

Direct numerical simulations of single-phase and multiphase viscoelastic fluid flows are performed in a square-shaped channel and the complex dynamics of the elasto-inertial turbulent regime are explored without introducing any explicit perturbations from outside the system. The bubble interfaces are fully resolved using a finite-difference/front-tracking method coupled with the Giesekus model equations to simulate chaotic flow regime of a shear-thinning viscoelastic fluid. Instead of using conventional numerical schemes to

discretise the constitutive equations by introducing artificial diffusion, a computationally expensive but robust log-conformation method is employed for the present DNS to preserve the integrity of EIT physics (Yerasi *et al.* 2024). The Reynolds number is varied by two orders of magnitude to cover a vast range below the threshold value of the inertial turbulence in the channel flow. Then, the Weissenberg number is varied by three orders of magnitude at each of these values of Reynolds numbers to explore the conditions for triggering transition to a turbulent regime in this rectilinear channel flow. Subsequently, unlike any previously tested methods, bubbles are injected into the flow under the conditions for which a single-phase flow remains fully laminar to check whether the presence of bubbles can trigger an instability to achieve the EIT flow regime. A constant flow rate is maintained corresponding to each Re by dynamically adjusting the applied pressure gradient. As different pathways can be followed in Re–Wi space to achieve EIT (Samanta *et al.* 2013), a concentrated polymer solution ($\beta = 0.1$) is considered in the present study for which the EIT regime is triggered much earlier than the inertial turbulence as the Reynolds number is increased.

It is observed that beyond $Wi \geqslant 100$, a single-phase flow becomes unstable when $Re \geqslant 100$. Fluctuations start to grow in this straight channel even without introducing any discrete external perturbations. These fluctuations propagate throughout the domain over time, ultimately leading to a fully chaotic flow field. The threshold value of Wi to trigger instability in the flow reduces with an increase in Re. For $Re = 1000$, the critical value of Wi to trigger the transition from laminar to turbulent state is found to be 50. When the value of Re is low ($Re = 10$), a Weissenberg number as high as 1000 cannot make the flow unstable. The energy spectra of this single-phase EIT regime reveal -4 scaling at the higher frequencies (dissipation range), while the classical $-5/3$ scaling is observed at the lower frequencies (inertial range) as the flow is dominated by both inertia as well as the elasticity.

It is found that if perturbed initially, single-phase viscoelastic flow cannot sustain a chaotic state in this rectilinear duct when $Wi \leqslant 40$ for all the three values of $Re = 1000$, 100 and 10 used in the present study.

A novel mechanism of achieving the EIT state by injecting the bubbles into the flow under the conditions for which a single-phase flow remains laminar is tested and verified at a Reynolds number as low as 10 and a Weissenberg number as low as 5. The curved streamlines across the bubble interfaces provide the necessary condition to trigger an instability even when the viscoelastic stresses are not very high and the single-phase flow remains completely laminar. The energy spectra shows a scaling of -2 for this low Wi multiphase EIT regime. It is found that this scaling is independent of size and the number of bubbles injected into the flow. Thus, it is concluded that the scaling of energy spectra varies from -4 to $-5/3$ depending upon the relative dominance of inertia and elasticity, i.e. -4 for a purely elastic turbulence and $-5/3$ for a purely inertial turbulence. All the other values of energy scaling would fall in between these two limits depending upon the relative strength of inertia (Re) and elasticity (Wi). It is also observed that the drag increases for all the situations where the laminar viscoelastic flow is fully transitioned to a turbulent state by injecting the bubbles into the flow. However, at the lower values of $Re = 10$ and 100, this higher value of skin friction drag of the EIT regime still remains lower than that of the corresponding laminar Newtonian flow for the same Reynolds number. Once the inertia and the elasticity are both low, the bubbles are aligned in the core region of the duct forming a string-shaped pattern ($Re = 10$, $Wi = 1$) or clusters ($Re = 100$, $Wi = 1$), and the flow remains laminar. For these cases, the friction drag reduces even further instead of increasing. Unlike the solid particles, it is found that a higher shear-thinning effect breaks up the alignment of bubbles.
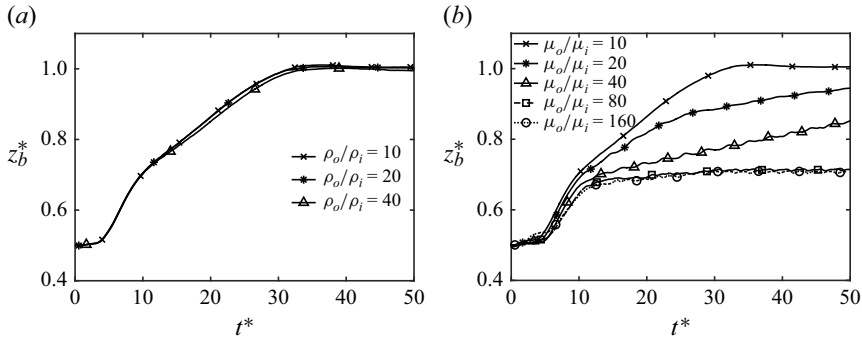
Figure 13. Effects of density and viscosity ratios. Evolution of a single bubble path in the wall-normal (z) direction in a concentrated polymer solution at (*a*) different density and at (*b*) different viscosity ratios ($Re = 10$, $Wi = 1$, $Ca = 0.01$, $\beta = 0.1$).

The idea of achieving the EIT state at a very low value of Re and Wi just by injecting the bubbles into the flow can find many potential applications involving processes where mixing, heat transfer or other transport phenomena are of primary importance. The present study would intrigue experimental verification as it has been demonstrated that the requirement of Wi to achieve the EIT state in a multiphase flow is low and realistic.

Declaration of interest. The authors declare no conflict of interest.

Data availability. Data can be shared upon request.

Appendix

Further simulations are performed to examine the effect of density and viscosity ratios on the multiphase flows considered in this study. For this purpose, the migration of a single bubble is examined in the pressure-driven viscoelastic channel flow, and the density and viscosity ratios are varied in the ranges of $10 \leqslant \rho_0/\rho_i \leqslant 40$ and $10 \leqslant \mu_o/\mu_i \leqslant 160$. The other parameters are fixed at $Re = 10$, $Wi = 1$, $Ca = 0.01$ and $\beta = 0.1$. The results are shown in figure 13. It is observed that the effects of density and viscosity ratios are negligible when $\rho_0/\rho_i \geqslant 10$ and $\mu_o/\mu_i \geqslant 80$, as seen in figures 13(*a*) and 13(*b*), respectively. Therefore, the density and viscosity ratios are set to $\rho_0/\rho_i = 10$ and $\mu_o/\mu_i = 80$ in all the results presented in this paper. In a concentrated polymer solution (e.g. $\beta = 0.1$), as considered in the present study, the viscosity ratio may have an impact on the bubble dynamics as the actual ratio can be as high as 10^8. However, it is shown here that beyond $\mu_o/\mu_i \geqslant 80$, the difference in the bubble path becomes less than 1 % (figure 13).

REFERENCES

AHMED, Z., IZBASSAROV, D., LU, J., TRYGGVASON, G., MURADOGLU, M. & TAMMISOLA, O. 2020 Effects of soluble surfactant on lateral migration of a bubble in a pressure driven channel flow. *Intl J. Multiphase Flow* **126**, 103251.

BENEITEZ, M., PAGE, J., DUBIEF, Y. & KERSWELL, R.R. 2024 Multistability of elasto-inertial two-dimensional channel flow. *J. Fluid Mech.* **981**, A30.

BENEITEZ, M., PAGE, J. & KERSWELL, R.R. 2023 Polymer diffusive instability leading to elastic turbulence in plane Couette flow. *Phys. Rev. Fluids* **8**, L101901.

BORGES, R., CARMONA, M., COSTA, B. & DON, W.S. 2008 An improved weighted essentially non-oscillatory scheme for hyperbolic conservation laws. *J. Comput. Phys.* **227**, 3191–3211.

BOTHE, D., NIETHAMMER, M., PILZ, C. & BRENN, G. 2022 On the molecular mechanism behind the bubble rise velocity jump discontinuity in viscoelastic liquids. *J. Non-Newtonian Fluid Mech.* **302**, 104748.

BUNNER, B. & TRYGGVASON, G. 2002 Dynamics of homogeneous bubbly flows Part 1. Rise velocity and microstructure of the bubbles. *J. Fluid Mech.* **466**, 17–52.

BUZA, G., PAGE, J. & KERSWELL, R.R. 2022 Weakly nonlinear analysis of the viscoelastic instability in channel flow for finite and vanishing Reynolds numbers. *J. Fluid Mech.* **940**, A11.

DALLAS, V., VASSILICOS, J.C. & HEWITT, G.F. 2010 Strong polymer-turbulence interactions in viscoelastic turbulent channel flow. *Phys. Rev. E* **82** (6), 066303.

DATTA, S.S. *et al.* 2022 Perspectives on viscoelastic flow instabilities and elastic turbulence. *Phys. Rev. Fluids* **7** (8), 080701.

DODD, M.S. & FERRANTE, A. 2014 A fast pressure-correction method for incompressible two-fluid flows. *J. Comput. Phys.* **273**, 416–434.

DONG, S. & SHEN, J. 2012 A time-stepping scheme involving constant coefficient matrices for phase-field simulations of two-phase incompressible flows with large density ratios. *J. Comput. Phys.* **231** (17), 5788–5804.

DUBIEF, Y., PAGE, J., KERSWELL, R.R., TERRAPON, V.E. & STEINBERG, V. 2022 First coherent structure in elasto-inertial turbulence. *Phys. Rev. Fluids* **7** (7), 073301.

DUBIEF, Y., TERRAPON, V.E. & HOF, B. 2023 Elasto-inertial turbulence. *Annu. Rev. Fluid Mech.* **55**, 675–705.

DUBIEF, Y., TERRAPON, V.E. & SORIA, J. 2013 On the mechanism of elasto-inertial turbulence. *Phys. Fluids* **25** (11), 110817.

DUBIEF, Y., WHITE, C.M., SHAQFEH, E.S.G. & TERRAPON, V.E. 2010 Polymer maximum drag reduction: a unique transitional state. In *Annual Research Briefs*, pp. 395–404.

FATTAL, R. & KUPFERMAN, R. 2005 Time-dependent simulation of viscoelastic flows at high Weissenberg number using the log-conformation representation. *J. Non-Newtonian Fluid Mech.* **126** (1), 23–37.

FOGGI ROTA, G., AMOR, C., LE CLAINCHE, S. & ROSTI, M.E. 2024 Unified view of elastic and elasto-inertial turbulence in channel flows at low and moderate Reynolds numbers. *Phys. Rev. Fluids* **9** (12), L122602.

GARG, P., CHAUDHARY, I., KHALID, M., SHANKAR, V. & SUBRAMANIAN, G. 2018 Viscoelastic pipe flow is linearly unstable. *Phys. Rev. Lett.* **121** (2), 024502.

GIESEKUS, H. 1982 A simple constitutive equation for polymer fluids based on the concept of deformation-dependent tensorial mobility. *J. Non-Newtonian Fluid Mech.* **11** (1–2), 69–109.

GROISMAN, A. & STEINBERG, V. 2000 Elastic turbulence in a polymer solution flow. *Nature* **405** (6782), 53–55.

IZBASSAROV, D., AHMED, Z., COSTA, P., VUORINEN, V., TAMMISOLA, O. & MURADOGLU, M. 2021*a* Polymer drag reduction in surfactant-contaminated turbulent bubbly channel flows. *Phys. Rev. Fluids* **6** (10), 104302.

IZBASSAROV, D. & MURADOGLU, M. 2015 A front-tracking method for computational modeling of viscoelastic two-phase flow systems. *J. Non-Newtonian Fluid Mech.* **223**, 122–140.

IZBASSAROV, D. & MURADOGLU, M. 2016*a*, A computational study of two-phase viscoelastic systems in a capillary tube with a sudden contraction/expansion. *Phys. Fluids* **28** (1), 012110.

IZBASSAROV, D. & MURADOGLU, M. 2016*b* Effects of viscoelasticity on drop impact and spreading on a solid surface. *Phys. Rev. Fluids* **1** (2), 023302.

IZBASSAROV, D., ROSTI, M.E., ARDEKANI, M.N., SARABIAN, M., HORMOZI, S., BRANDT, L. & TAMMISOLA, O. 2018 Computational modeling of multiphase viscoelastic and elastoviscoplastic flows. *Intl J. Numer. Meth. Fluids* **88** (12), 521–543.

IZBASSAROV, D., ROSTI, M.E., BRANDT, L. & TAMMISOLA, O. 2021*b* Effect of finite Weissenberg number on turbulent channel flows of an elastoviscoplastic fluid. *J. Fluid Mech.* **927**, A45.

LELLEP, M., LINKMANN, M. & MOROZOV, A. 2024 Purely elastic turbulence in pressure-driven channel flows. *Proc. Natl Acad. Sci. USA* **121** (9), e2318851121.

LI, G., MCKINLEY, G.H. & ARDEKANI, A.M. 2015 Dynamics of particle migration in channel flow of viscoelastic fluids. *J. Fluid Mech.* **785**, 486–505.

MCKINLEY, G.H., PAKDEL, P. & ÖZTEKIN, A. 1996 Rheological and geometric scaling of purely elastic flow instabilities. *J. Non-Newtonian Fluid Mech.* **67**, 19–47.

MOROZOV, A. & VAN SAARLOOS, W. 2019 Subcritical instabilities in plane Poiseuille flow of an Oldroyd-B fluid. *J. Stat. Phys.* **175**, 554–577.

MOROZOV, A.N. & VAN SAARLOOS, W. 2005 Subcritical finite-amplitude solutions for plane Couette flow of viscoelastic fluids. *Phys. Rev. Lett.* **95** (2), 024501.

MUKHERJEE, S., SINGH, R.K., JAMES, M. & RAY, S.S. 2023 Intermittency, fluctuations and maximal chaos in an emergent universal state of active turbulence. *Nat. Phys.* **19** (6), 891–897.

NASEER, H.U., AHMED, Z., IZBASSAROV, D. & MURADOGLU, M. 2023 Dynamics and interactions of parallel bubbles rising in a viscoelastic fluid under buoyancy. *J. Non-Newtonian Fluid Mech.* **313**, 105000.

NASEER, H.U., IZBASSAROV, D., AHMED, Z. & MURADOGLU, M. 2024 Lateral migration of a deformable fluid particle in a square channel flow of viscoelastic fluid. *J. Fluid Mech.* **996**, A31.

OWOLABI, B.E., POOLE, R.J. & DENNIS, D.J.C. 2016 Experiments on low-Reynolds-number turbulent flow through a square duct. *J. Fluid Mech.* **798**, 398–410.

PTASINSKI, P.K., NIEUWSTADT, F.T.M., VAN DEN BRULE, B.H.A.A. & HULSEN, M.A. 2001 Experiments in turbulent pipe flow with polymer additives at maximum drag reduction. *Flow Turbul. Combust.* **66**, 159–182.

SAMANTA, D., DUBIEF, Y., HOLZNER, M., SCHÄFER, C., MOROZOV, A.N., WAGNER, C. & HOF, B. 2013 Elasto-inertial turbulence. *Proc. Natl Acad. Sci. USA* **110** (26), 10557–10562.

SCHLEINIGER, G. & WEINACHT, R.J. 1991 A remark on the Giesekus viscoelastic fluid. *J. Rheol.* **35** (6), 1157–1170.

SHAHMARDI, A., ZADE, S., ARDEKANI, M.N., POOLE, R.J., LUNDELL, F., ROSTI, M.E. & BRANDT, L. 2019 Turbulent duct flow with polymers. *J. Fluid Mech.* **859**, 1057–1083.

SID, S., TERRAPON, V.E. & DUBIEF, Y. 2018 Two-dimensional dynamics of elasto-inertial turbulence and its role in polymer drag reduction. *Phys. Rev. Fluids* **3** (1), 011301.

SINGH, R.K., PERLEKAR, P., MITRA, D. & ROSTI, M.E. 2024 Intermittency in the not-so-smooth elastic turbulence. *Nat. Commun.* **15** (1), 4070.

STEINBERG, V. 2021 Elastic turbulence: an experimental view on inertialess random flow. *Annu. Rev. Fluid Mech.* **53**, 27–58.

TRYGGVASON, G., BUNNER, B., ESMAEELI, A., JURIC, D., AL-RAWAHI, N., TAUBER, W., HAN, J., NAS, S. & JAN, Y.-J. 2001 A front-tracking method for the computations of multiphase flow. *J. Comput. Phys.* **169** (2), 708–759.

TRYGGVASON, G., SCARDOVELLI, R. & ZALESKI, S. 2011 *Direct Numerical Simulations of Gas–Liquid Multiphase Flows*. Cambridge University Press.

UNVERDI, S.O. & TRYGGVASON, G. 1992 A front-tracking method for viscous, incompressible, multi-fluid flows. *J. Comput. Phys.* **100** (1), 25–37.

VARCHANIS, S., HAWARD, S.J., HOPKINS, C.C., TSAMOPOULOS, J. & SHEN, A.Q. 2022 Evaluation of constitutive models for shear-banding wormlike micellar solutions in simple and complex flows. *J. Non-Newtonian Fluid Mech.* **307**, 104855.

WAN, D., SUN, G. & ZHANG, M. 2021 Subcritical and supercritical bifurcations in axisymmetric viscoelastic pipe flows. *J. Fluid Mech.* **929**, A16.

WON, D. & KIM, C. 2004 Alignment and aggregation of spherical particles in viscoelastic fluid under shear flow. *J. Non-Newtonian Fluid Mech.* **117** (2–3), 141–146.

YERASI, S.R., PICARDO, J.R., GUPTA, A. & VINCENZI, D. 2024 Preserving large-scale features in simulations of elastic turbulence. *J. Fluid Mech.* **1000**, A37.

YOO, J.Y. & CHOI, H.C. 1989 On the steady simple shear flows of the one-mode Giesekus fluid. *Rheol. Acta* **28**, 13–24.